Flux closures and source term models for shallow water models with depth-dependent integral porosity

Vincent Guinot, C. Delenne, Antoine Rousseau, O. Boutron

Flux closures and source term models for shallow water models with depth-dependent integral porosity

V. Guinot (1,2), C. Delenne (1,2), A. Rousseau (2,3), O. Boutron (4)

(1) HSM, Univ. Montpellier, CNRS, IRD, Montpellier, France
(2) LEMON, Inria, Montpellier, France
(3) IMAG, CNRS, Univ. Montpellier, Montpellier, France
(4) Tour du Valat Research Institute, Arles, France

This is the preprint of a manuscript accepted for publication in Advances in Water Resources.
Publisher's version: DOI https://doi.org/10.1016/j.advwatres.2018.09.014

Abstract

A two-dimensional shallow water model with depth-dependent porosity is presented. The purpose is the coarse grid simulation of shallow flows over complex topographies and geometries. Two flux closures are examined: the Integral Porosity (IP) and Dual Integral Porosity (DIP) closures. Energy losses are described using a subgrid scale model that accounts for bottom and wall friction, transient momentum dissipation and energy losses induced by obstacle submersion. A complete wave propagation property analysis is provided for the IP and DIP closures, yielding more accurate numerical stability constraints than published previously. Five computational examples are presented, including transients in compound and meandering channels, urban dambreak problems with building submersion and runoff over variable microtopography. The ability of the model to deal with subgrid-scale features is confirmed. The DIP flux is shown to be superior to the IP closure. The transient dissipation term is essential in reproducing the effect of obstacles and microtopography. Distinguishing between the building wall- and building roof-induced friction is seen to be essential. The model is validated successfully against a scale model experimental dataset for the submersion of a coastal urban area by a tsunami wave.

Keywords Flood modelling; shallow water model; upscaling; porosity model; flux closure; source term

1 Introduction

Over the past decade, porosity-based shallow water models have become increasingly popular in dealing with subgrid-scale geometric and topographic features in shallow water flows. Typical applications include urban flood modelling and the modelling of shallow flows over complex topographies [1, 13]. In the Single Porosity (SP) approach, a single porosity is used to account for both the storage and the connectivity properties of the subgrid-scale geometry. While early developments [1, 13] used a depth-dependent SP field, most of the developments and applications of the SP approach presented to date have focused on depth-independent SP versions of the shallow water equations [2, 8, 15, 17, 21, 25, 38, 42, 47]. This restriction of the original approach is easily justified by the fact that these models were developed for urban flood modelling purposes, where the buildings are assumed not to be submerged by the flood in practice. One of the main limitations of the original SP approach [13] is that it does not allow anisotropy effects to be accounted for. Two ways of introducing anisotropy effects using the SP approach are known so far from the literature. In the Multiple Porosity (MP) model [21], the flow region is broken into several subregions, each having its own, single porosity. Some of the regions are applied momentum corrections to account for preferential flows and stagnant water

in dead zones. More recently, anisotropy is incorporated directly in the flux functions of the SP model [48].

The Integral Porosity (IP) approach [38, 39], originally designed for urban flood modelling, incorporates anisotropy by defining two types of porosity: a storage (or areal) porosity and a connectivity (or frontal) porosity. The storage and connectivity porosities express the statistical properties of the urban geometry over the domain of interest and its boundary respectively. While the storage porosity does not include information on the anisotropy of the geometry, the connectivity porosity does because it is a function of the orientation of the boundary. The IP approach has been extended to depth-dependent porosity fields [34, 35]. The Building Coverage Ratio/Conveyance Reduction Factor (BCR/CRF) approach [10, 11] also uses two statistical indicators of the urban geometry that act in a similar fashion to that of the storage and conveyance porosities. The multilayer definition [11] makes the approach very similar to that of the MP model. The IP and BCR/CRF approaches share the common feature that they allow the influence of buildings on the wave propagation speeds to be accounted for. Such effects are also obtained by including multiple flow regions, as in [21, 32].

The Dual Integral Porosity (DIP) model [24] has been proposed as an improved version of the IP model. The accuracy of the fluxes is improved by enforcing mass flux invariance between the interior points of the domain and the boundaries. The superiority of the DIP model over the IP has been confirmed by numerical experiments involving the comparison of the IP and DIP models to shallow water solutions obtained on refined grids [24, 23]. The IP model is known to underestimate the wave propagation speeds of transients in the presence of obstacles, a drawback that is eliminated to a large extent by the DIP model. A depth-independent porosity model derived from independent considerations [6] has also been shown to achieve improved wave propagation properties when made consistent with the DIP fluxes. The DIP model also incorporates a transient momentum dissipation mechanism, active only for positive waves. A consistency analysis of the IP and DIP equations indicates that the DIP model is less sensitive to the design of the computational grid than is the IP model [22]. Moreover, benchmarking the SP, IP and DIP models against a simulation base of 96 scenarios shows that the DIP gives the more accurate mass and momentum fluxes of the three models, although some issues remain when the geometry is strongly anisotropic and exhibits preferential directions [23]. So far, however, the DIP model has been developed and applied only for depth-independent porosity fields.

The purpose of the present paper is to present a shallow water model based on the DIP approach, with depth-variable porosity fields. This model is called the Depth-Dependent Porosity (DDP) model hereafter. It has several novel features: (i) the DIP closure presented in [24] is generalized to depth-dependent storage and connectivity porosities, (ii) the transient momentum dissipation model and the drag source term models are adapted to reflect the possible submersion of the topography by the flow (a feature that is absent from the original DIP model), (iii) the governing equations are discretized over unstructured grids (while [6, 35, 34] involve only rectangular or square grids), (iv) the depth-dependent porosity laws can be made totally arbitrary and be discretized with an arbitrary degree of accuracy.

This paper is organized as follows. Section 2 presents the underlying assumptions and governing equations of the model. Section 3 details the discretization of the fluxes and source terms in the framework of an explicit, shock-capturing discretization, as well as the CFL stability constraint. Section 4 presents five test cases devoted to the verification and validation of specific features of the proposed model. Section 5 presents a validation of the model against scale model experiments. Sections 6 and 7 are devoted respectively to a discussion and conclusions.

2 Model

2.1 Depth-dependent porosity laws

The purpose is to model two-dimensional shallow water flows over a solid, non-erodible topography, that is, in the presence of an impermeable bottom, with a bottom level field $z_b(x,y)$ that is a function only of the horizontal coordinates (x,y). Consider a two-dimensional domain Ω with boundary Γ, normal unit vector $\mathbf{n}$ in the (x,y) plane. Such a domain may be e.g. a cell in a computational mesh, but may also be any arbitrary-shaped domain. A phase indicator $\varepsilon(x,y,z)$ is defined as follows: $\varepsilon(x,y,z)=0$ if the point (x,y,z) is in the solid phase, $\varepsilon(x,y,z)=1$ otherwise. The phase indicator is a purely geometric descriptor. A such, it is independent of the flow field. Two porosities ϕ_Ω and ϕ_Γ are

defined respectively for the domain and its boundary. They represent the amount of water that can be stored per unit domain and boundary respectively for a unit variation in the free surface elevation z_s. Assuming that the function $z_s(x,y)$ is known, storage and connectivity porosities are defined as

$$\phi_\Omega(z_\Omega) = \frac{1}{\Omega}\int_\Omega \varepsilon(x,y,z_s(x,y))\,\mathrm{d}\Omega \tag{1a}$$

$$\phi_\Gamma(z_\Gamma) = \frac{1}{\Gamma}\int_\Gamma \varepsilon(x,y,z_s(x,y))\,\mathrm{d}\Gamma \tag{1b}$$

$$z_D = \frac{\int_D z_s(x,y)\,\varepsilon(x,y,z_s(x,y))\;\mathrm{d}D}{\int_D \varepsilon(x,y,z_s(x,y))\,\mathrm{d}D},\quad D=\Omega,\Gamma \tag{1c}$$

Note that equation (1c) is valid as long as the integral of $\varepsilon(x,y,z_s(x,y))$ is non-zero, that is, as long as D includes a subdomain with non-zero measure where there is a free surface. If the entire domain is filled with the solid phase, $\varepsilon = 0$ everywhere and both the numerator and denominator of the ratio (1c) are zero. In this case, D being entirely dry, it can be considered not being a part of the flow domain and the computation of z_D becomes meaningless.

The average elevation $z_D(D=\Omega,\Gamma)$ defined in Equation (1c) depends directly on the subgrid-scale free surface elevation function $z_s(x,y)$. Consequently, the functions $\phi_\Omega(z_\Omega)$ and $\phi_\Gamma(z_\Gamma)$ are not unique in the general case. Consider the simple example of a uniform bottom slope in the $x-$direction (Figure 1) with a given z_Ω. In Figure 1a, the free surface is horizontal, below the upper bound of the bottom elevation over Ω (as for e.g. water at rest in a pond). The domain is partially dry, which results in $\phi_\Omega < 1$, and $\phi_\Gamma = 0$ along the right-hand boundary. In Figure 1b, the free surface is tilted, roughly parallel to the bottom (as in the case of e.g. runoff over a steep slope). This results in $\varepsilon = 1$ at all points in Ω and consequently $\phi_\Omega = 1$. The boundary porosity ϕ_Γ is also equal to unity at the right-hand boundary. While z_Ω is identical in both situations, the porosity ϕ_Ω is not.

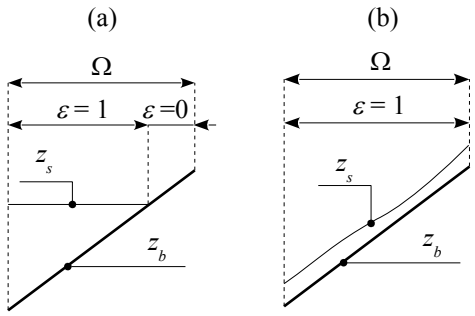

Figure 1: Depth-dependent porosity. Definition sketch for two different free surface profiles.

This simple example shows that the porosity ϕ_D is not a single-valued function of z_D because different ϕ_D values may be computed for a given average water level z_D depending on the shape of the free surface on the subgrid scale. Laws in the form $\phi_D(z_D)$, $D=\Omega,\Gamma$ are thus meaningful only provided that a subgrid-scale model for the free surface elevation is specified. It is worth noting that, in the first presentation of a depth-dependent porosity model by Defina [13], two different $z_s(x,y)$ models were implicitly assumed. For the Venice lagoon application, a model similar to that of Figure 1a was used, while for the runoff simulations, sheet flow with a free surface roughly parallel to the mean bottom surface is assumed, which corresponds to Figure 1b.

The developments presented hereafter are based on the assumption that the free surface is nearly horizontal, therefore $z_s(x,y)$ is independent of x and y, thus $z_\Omega = z_\Gamma$ over the domain Ω. In this case, the porosities ϕ and their integrals θ become single-valued functions of the vertical coordinate z_D $(D=\Omega,\Gamma)$. Since the elevations $z_s(x,y) = z_\Omega = z_\Gamma$ are identical, they can be replaced with the same argument z in Equations (1a-1c). This yields the following formulae for the porosities and their integrals

$$\phi_D(z) = \frac{1}{D}\int_D \varepsilon(x,y,z)\,\mathrm{d}D,\quad D=\Omega,\Gamma \tag{2a}$$

$$\theta_D(z) = \int_{z_b}^{z} \phi_D(\zeta)\,\mathrm{d}\zeta, \quad D = \Omega, \Gamma \tag{2b}$$

$$0 \leq \phi_\Gamma(z) \leq \phi_\Omega(z)\,\forall z \tag{2c}$$

$$0 \leq \theta_\Gamma(z) \leq \theta_\Omega(z)\,\forall z \tag{2d}$$

Equation (2c) stems from the assumption that the connectivity porosity is smaller than the storage porosity by definition [38]. Equation (2d) is obtained directly by integrating (2c) with respect to z.

In the present work, the laws $\phi_D(z)$ $(D = \Gamma, \Omega)$ are derived from statistical properties of the topography. Consequently, their support is assumed to have a lower bound $z_{b,D}$. Note that this is not the case in all approaches. In [13, 48], an error function-based law is used, and ϕ_D is non-zero even for elevations lower than the lowest point within the sampling domain. While physically unrealistic, such laws have the advantage that they allow wetting/drying issues to be eliminated. This is an advantage when numerical methods particularly sensitive to wetting/drying issues are used, as e.g. Galerkin finite element methods [13, 48].

2.2 Mass conservation

A mass balance over Ω yields

$$\mathrm{d}_t V + Q = 0 \tag{3}$$

where V and Q are respectively the volume of water in Ω and the outflowing discharge across the boundary. As in [13], V is obtained by integrating ε over the cylinder with base surface Ω extending from z_b to z_s

$$V = \int_{z_b}^{z_s} \int_\Omega \varepsilon \mathrm{d}\Omega\,\mathrm{d}z = \Omega \int_{z_b}^{z_s} \phi_\Omega(z)\,\mathrm{d}z = \Omega\theta_\Omega(z_s) \tag{4}$$

The discharge Q is obtained by integrating the normal flow velocity over the boundary of the same cylinder

$$Q = \int_{z_b}^{z_s} \int_\Gamma \varepsilon \mathbf{u}.\mathbf{n}\mathrm{d}\Gamma\,\mathrm{d}z = \int_\Gamma \theta_\Gamma \mathbf{u}.\mathbf{n}\mathrm{d}\Gamma = \int_\Gamma \mathbf{q}_\Gamma.\mathbf{n}\mathrm{d}\Gamma \tag{5}$$

where $\mathbf{q}_\Gamma = \theta_\Gamma \mathbf{u}$ is the unit discharge vector at the boundary. This boundary unit discharge is related to the domain-averaged unit discharge via a closure model presented in Subsection 2.4. Substituting (4,5) into (3) yields

$$\mathrm{d}_t(\Omega\theta_\Omega) + \int_\Gamma \mathbf{q}_\Gamma.\mathbf{n}\,\mathrm{d}\Gamma = 0 \tag{6}$$

2.3 Momentum conservation

The underlying assumptions of the shallow water model are retained: the flow velocity field is assumed nearly horizontal, the slopes and curvature of the bottom and free surface are assumed small, leading to a hydrostatic pressure field. Applying Newton's second law of motion to the domain yields

$$\mathrm{d}_t \int_{z_b}^{z_s} \int_\Omega \varepsilon \mathbf{u}\mathrm{d}\Omega\,\mathrm{d}z + \int_{z_b}^{z_s} \int_\Gamma \varepsilon(\mathbf{u}.\mathbf{n})\mathbf{u}\mathrm{d}\Gamma\,\mathrm{d}z = \mathbf{f}_w + \mathbf{f}_s + \mathbf{f}_f \tag{7}$$

where $\mathbf{f}_f, \mathbf{f}_w, \mathbf{f}_s$ are respectively the specific forces stemming from friction and drag, the hydrostatic pressure exerted by the water along the boundary and the reaction from the solid phase to the pressure force along the solid-liquid interface within the domain Ω (Figure 2). Figure 2 shows a horizontal slice of height $\mathrm{d}z$ drawn at an elevation z.

The pressure force $\mathbf{f}_w$ is active only along the part of the boundary in the water phase, that is, only at the boundary points with $\varepsilon = 1$:

$$\mathbf{f}_w = -\int_{z_b}^{z_s} \int_\Gamma \varepsilon g(z_s - z)\,\mathbf{n}\mathrm{d}\Gamma\,\mathrm{d}z \tag{8}$$

where g is the gravitational acceleration. Since the porosity ϕ_Γ is considered in a statistical sense as the mathematical expectation of ε over Γ, the following property is assumed to hold

$$\int_\Gamma \varepsilon g(z_s - z)\,\mathrm{d}\Gamma = \int_\Gamma \phi_\Gamma g(z_s - z)\,\mathrm{d}\Gamma \tag{9}$$

because the hydrostatic pressure field $p = g\,(z_s - z)$ is assumed uncorrelated with the phase indicator ε. Inserting the above expression into Equation (8), swapping the integrals yields

$$\mathbf{f}_w = -\int_\Gamma \int_{z_b}^{z_s} \phi_\Gamma\,(z)\, g\,(z_s - z)\,\mathrm{d}z\,\mathbf{n}\mathrm{d}\Gamma \tag{10}$$

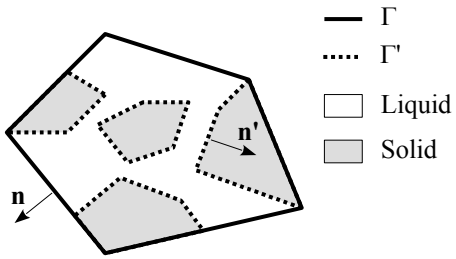

Figure 2: Momentum balance. Definition sketch for a given elevation z.

The reaction from the solid-liquid interface accounts for the effects of topography. This includes the bottom slope, as well as emergent vertical surfaces such as building walls in the presence of buildings, etc.

$$\mathbf{f}_s = -\int_{z_b}^{z_s} \int_{\Gamma'} \varepsilon g\,(z_s - z)\,\mathbf{n}'\mathrm{d}\Gamma'\,\mathrm{d}z \tag{11}$$

where the shape and extension of Γ' varies with z. It is not possible to find a general expression for the above integral for an arbitrary obstacle distribution. The following model is proposed hereafter: the density of solid obstacles is assumed the same along the boundary Γ as within the domain Ω. Since the free surface is assumed horizontal (Equation (2a)), the pressure force stemming from the reaction along solid/liquid interfaces entirely contained within the domain (as the central island in Figure 2) is zero and only the pressure force onto the solid/liquid interface at the boundary remains. The balance of the pressure forces along the boundary is obtained by isolating a small domain delineated by a boundary segment $\mathrm{d}\Gamma$, extending by an infinitesimal length $\mathrm{d}l$ into the domain (Figure 3).

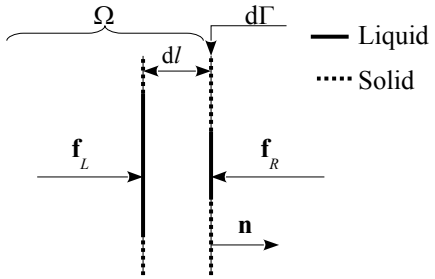

Figure 3: Pressure force balance. Definition sketch.

In the limit $\mathrm{d}l \to 0$, one has

$$\mathrm{d}\mathbf{f}_s + \mathrm{d}\mathbf{f}_L + \mathrm{d}\mathbf{f}_R = 0 \tag{12}$$

where $\mathrm{d}\mathbf{f}_L$ and $\mathrm{d}\mathbf{f}_R$ are respectively the pressure forces exerted onto the left- and right-hand sides of the control volume:

$$\mathrm{d}\mathbf{f}_L = \int_{z_b}^{z_s} \varepsilon g\,(z_s - z)\,\mathbf{n}\mathrm{d}z\,\mathrm{d}\Gamma \Rightarrow \mathbf{f}_L = \int_\Gamma \int_{z_b}^{z_s} \phi_\Omega g\,(z_s - z)\,\mathbf{n}\mathrm{d}z\,\mathrm{d}\Gamma \tag{13a}$$

$$\mathrm{d}\mathbf{f}_R = -\int_{z_b}^{z_s} \varepsilon g\,(z_s - z)\,\mathbf{n}\mathrm{d}z\,\mathrm{d}\Gamma \Rightarrow \mathbf{f}_R = -\int_{z_b}^{z_s} \phi_\Gamma g\,(z_s - z)\,\mathbf{n}\mathrm{d}z\,\mathrm{d}\Gamma \tag{13b}$$

Note that ϕ_Ω and ϕ_Γ are used respectively for $\mathbf{f}_L$ and $\mathbf{f}_R$ because $\mathbf{f}_L$ is exerted onto a surface that is located within Ω, while $\mathbf{f}_R$ is exerted onto a surface that belongs to Γ. The following expression is obtained for the pressure force:

$$\mathbf{f}_s = -\mathbf{f}_L - \mathbf{f}_R = -\int_\Gamma \int_{z_b}^{z_s} (\phi_\Omega - \phi_\Gamma)\, g\,(z_s - z)\,\mathbf{n}\mathrm{d}z\,\mathrm{d}\Gamma \tag{14}$$

The friction force is assumed to result from both friction against the bottom and head losses stemming from the presence of obstacles obstructing the flow within the domain Ω.

$$\mathbf{f}_f = -\int_{z_b}^{z_s} \int_\Omega \varepsilon g \mathbf{s}_f \mathrm{d}\Omega\,\mathrm{d}z = -\int_\Omega g\theta_\Omega \mathbf{s}_f \mathrm{d}\Omega \tag{15}$$

where g is the gravitational acceleration and $\mathbf{s}_f$ is the energy slope vector. Various formulations have been proposed for $\mathbf{s}_f$ [18, 25, 24, 38, 34]. Numerical experiments and simulations of field-scale hydraulic transients show that energy losses are best described by introducing two types of momentum source terms [24]. The first is a steady-sate, turbulent source term arising from bottom friction and building drag. The second is a momentum dissipation source term active only under transient conditions involving positive waves. This momentum dissipation source term accounts for the dissipation of moving bores arising from the positive waves into dead zones or low velocity areas. The following formulae are used in the DIP model [24]:

$$\mathbf{f}_f = \mathbf{f}_b + \mathbf{f}_D + \mathbf{f}_T \tag{16a}$$

$$\mathbf{f}_b = -\int_\Omega g n_M^2 \frac{\theta_\Omega}{h_\Omega^{4/3}} |\mathbf{u}|\,\mathbf{u}\mathrm{d}\Omega, \quad h = z_s - z_b \tag{16b}$$

$$\mathbf{f}_D = -\int_\Omega g \mathbf{C}_D\,|\mathbf{u}|\,\mathbf{u}\mathrm{d}\Omega \tag{16c}$$

$$\mathbf{f}_T = -\mathbf{M}\left(\int_{z_b}^{z_s}\int_\Gamma \phi_\Gamma\,(\mathbf{u}.\mathbf{n})\,\mathbf{u}\mathrm{d}\Gamma\,\mathrm{d}z - \mathbf{f}_w\right) \tag{16d}$$

$$\mathbf{M} = \begin{cases} \begin{bmatrix} 0 & 0 & 0 \\ 0 & \mu_{xx} & \mu_{xy} \\ 0 & \mu_{yx} & \mu_{yy} \end{bmatrix} & \text{if} \quad \partial_t h > 0 \\ 0 & \text{if} \quad \partial_t h \leq 0 \end{cases} \tag{16e}$$

where $\mathbf{f}_b$, $\mathbf{f}_D$ and $\mathbf{f}_T$ are respectively the bottom friction, the drag and transient momentum dissipation terms, h is the water depth, n_M is Manning's friction coefficient, $\mathbf{C}_D$ is the building drag tensor, and the coefficients $\mu_{ij}(i,j=x,y)$ are momentum dissipation coefficients between zero and unity. The transient momentum dissipation model was first introduced in [24] and its existence and expression have been validated using refined two-dimensional flow simulations [23]. The drag and transient source terms used in the present model are modified versions of the models presented and used in [24, 23, 35, 34, 38, 39]. The modified models are presented in Subsection 2.5.

2.4 Domain/boundary closure model

IP closure. The IP model [38] uses the following closure model

$$z_{s,\Gamma} = z_{s,\Omega} \tag{17a}$$

$$\mathbf{u}_\Gamma = \mathbf{u}_\Omega \tag{17b}$$

This closure is shown to violate mass conservation across the boundary and yield erroneous wave propagation speeds [24].

DIP closure. The DIP model [24] was proposed as a correction to the IP closure:

$$z_{s,\Gamma} = z_{s,\Omega} \tag{18a}$$

$$\mathbf{u}_\Gamma = \frac{\phi_\Omega}{\phi_\Gamma}\mathbf{u}_\Omega \tag{18b}$$

with the necessary condition $\phi_\Gamma \leq \phi_\Omega$ for problem well-posedness. The DIP closure is seen to provide more accurate solutions than the IP model [6, 24] and to be less sensitive to the design of the mesh [22]. Transposing this closure to the present depth-variable model gives

$$z_{s,\Gamma} = z_{s,\Omega} \tag{19a}$$

$$\mathbf{u}_\Gamma = \frac{\theta_\Omega}{\theta_\Gamma}\mathbf{u}_\Omega, \;\; \theta_\Gamma \leq \theta_\Omega \tag{19b}$$

However, this definition poses problems in the case of water tending to the minimum level for ϕ_Γ, because it yields an infinite speed $\mathbf{u}_\Gamma$ as the water level reaches the elevation for which $\theta_\Gamma = 0$. This clearly induces a violation of the principle of conservation of energy, because the kinetic term $\|\mathbf{u}_\Gamma\|^2/(2g)$ tends to infinity over Γ while it is finite within Ω. Energy would thus increase along a streamline from a finite value within Ω to an infinite value over Γ. This non-physical behaviour is eliminated using an energy-based limiting of the flow velocity. When the water depth at the boundary drops below a given predefined value $h_{\min}$, the normal flow velocity is bounded by the maximum possible value $u_{\max}$ that satisfies energy invariance along a streamline:

$$2gz_{s,\Omega} + u_\Omega^2 = 2gz_{s,\Gamma} + u_\Gamma^2 \tag{20}$$

The maximum permissible value for u_Γ is obtained by setting $z_{s,\Gamma}$ to its minimum possible value, that is, $z_{\Gamma,\min}$. The flow velocity at the boundary is limited as follows

$$z_{s,\Gamma} \leq z_{\Gamma,\min} + h_{\min} \Rightarrow u_{\Gamma,n} \mapsto \max\left(-u_{\max}, \min\left(u_{\Gamma,n}, u_{\max}\right)\right) \tag{21a}$$

$$u_{\max} = \left(\max\left(0, \left(z_{s,\Omega} - z_{\Gamma,\min}\right)2g + u_{\Omega,n}^2\right)\right)^{\frac{1}{2}} \tag{21b}$$

$$u_{\Omega,n} = \mathbf{u}_\Omega.\mathbf{n}, \;\; u_{\Gamma,n} = \mathbf{u}_\Gamma.\mathbf{n} \tag{21c}$$

where $z_{\Gamma,\min}$ is the lower bound of the support of $\phi_\Gamma(z)$. The formula (21b) for $u_{\max}$ is obtained by applying Bernoulli's theorem along a streamline connecting the interior points of Ω to Γ. The maximum possible value for the velocity is achieved by setting $z_{s,\Gamma} = z_{\Gamma,\min}$ in Equation (21b). For all the applications presented in this paper, $h_{\min}$ is set to 10^{-3}m. Note that this problem is not met in the depth-independent DIP model [24], where θ is replaced with ϕ (that is assumed non-zero).

2.5 Momentum source terms

The purpose of the present section is to propose a momentum source term that can be used in two types of situations. The first is the modelling of urban floods, with the eventuality that obstacles (such as vehicles, but also possibly houses or buildings) may be submerged. The second is the modelling of flows over strongly variable topography, that may be only partially or fully submerged. This is a major upscaling challenge, in that the purpose is to cover a wide range of flow configurations and regimes.

As far as the bottom friction model (16b) is concerned, a constant n_M as used in Equation (16b) is deemed insufficient. The effect of rainfall and small water depths are known to influence the roughness coefficient significantly [7, 18, 27, 44]. Experimental studies indicate threshold effects with respect to the water depth and Reynolds number for the roughness coefficient, with a predominant effect of the Reynolds number [18]. Moreover, the effects of surface roughness on free surface flows have been identified to depend strongly on the inundation ratio Λ [31], that is the ratio of the flow depth to the characteristic roughness scale. In [31], a three-stage behaviour is proposed for the resistance model: when the flow is shallower than the characteristic roughness scale (the so-called partial inundation range), the friction factor follows a drag force law and is proportional to the inundation ratio. In the marginal inundation range (when Λ is of the order of magnitude of unity), the resistance factor transitions from the drag model to a mixing length model, where the friction factor is proportional to $\Lambda^{-1/2}$. For well-inundated flow ($\Lambda > 10$), roughness models such as Colebrook-type laws are valid.

Acknowledging the salient importance of the inundation ratio Λ, upscaled roughness formulations have been proposed with inundation ratio-dependent Manning coefficients [36].

Concerning the modelling of building drag forces, a general formulation is still to be proposed. In [38, 39, 35, 34], isotropic models based on drag coefficient or Chezy-Manning laws are used. A number of these models are inspired from formulae on vegetation-induced drag forces. A large body of literature is available for the study of drag forces induced by submerged or emergent vegetation (see e.g. [9, 14, 33, 40]). However, the urban context is very specific in that a strong anisotropy is often observed in terms of building layout, shape and alignment. Isotropic drag formulae are not sufficient in such situations. They were generalized into the tensor formulation (16c) in [24]. A similar tensor formulation is presented in [6], with the simplification that the computational grid is Cartesian and the principal directions of the drag tensor are assumed aligned with those of the grid. As a consequence of this simplification, the drag tensor is very sensitive to the flow directions (see subsection 4.2.4 in [6]). A more general approach has been introduced by Velickovic et al. [47]. The tensor formulation arises as a particular case of this approach. Velickovic et al.'s model has the advantage that it allows directions of minimal head loss to be easily incorporated in the drag model, a feature that the tensor formulation does not handle. However, in [23], systematic, refined 2D flow simulations over idealized street networks are shown to invalidate all previously proposed drag models (including [47]) when the flow is not aligned with the main directions of the street network.

Lastly, in [23, 24], numerical experiments dealing with the propagation of simple waves in idealized urban networks provide evidence for the existence of an additional dissipation mechanism in the refined 2D shallow water solutions. This mechanism is active only under transient conditions involving the propagation of positive waves. It is attributed to the dissipation of shocks and multiple wave reflections onto the building walls when a positive flood wave propagates into the urban layout. In contrast with the drag force $\mathbf{f}_D$, the transient term $\mathbf{f}_T$ does not obey an equation of state with respect to the flow variables. It acts on the inertia of the water phase via the dissipation tensor $\mathbf{M}$ in Equations (16d-16e). When the flow is aligned with the main directions of the street network, this dissipation model alone suffices to reproduce the momentum losses observed in the refined 2D model [23, 24], without the need for additional terms. Attempting to reproduce the effects of the term $\mathbf{f}_T$ using an artificially increased drag coefficient only contributes to degrade the accuracy of the porosity solution [24].

Bearing in mind that all drag models are inaccurate when the flow is not aligned with the main directions of the obstacles, the purpose here is to provide a source term model that provides satisfactory results at least when the flow is aligned with the main directions of the geometry. While intentionally limited, the objective is to propose a model with minimal complexity that allows the main features of the flow to be reproduced. The generalisation of the model to account for arbitrarily complex flow features is clearly beyond the scope of the present work. It is left for future research.

The proposed source term model is assumed to arise from three mechanisms, illustrated by Figure 4.

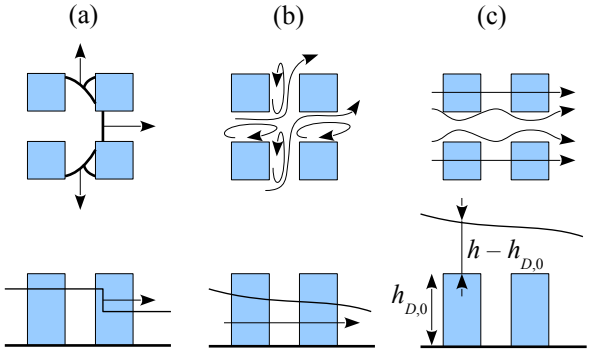

Figure 4: The three momentum dissipation mechanisms. a: Transient, positive wave dissipation (term $\mathbf{f}_T$). b: drag induced by obstacle walls (term $\mathbf{f}_{D,1}$). c: drag induced by obstacle overflow (term $\mathbf{f}_{D,2}$). Top: plan view. Bottom: side view.

The first mechanism is the transient momentum dissipation mechanism (Figure 4a), active only in the presence of positive waves (rising water levels). Since the dissipation arises from the multiple

wave reflections against the obstacle walls, the source term takes effect only over the smaller of the two depths $h, h_{D,0}$, where $h_{D,0}$ is the height of the obstacles. The source term (16d) is thus revised into

$$\mathbf{f}_T = -\frac{\min(h, h_{D,0})}{h}\mathbf{M}\left(\int_{z_b}^{z_s}\int_{\Gamma}\epsilon\,(\mathbf{u}.\mathbf{n})\,\mathbf{u}\mathrm{d}\Gamma\,\mathrm{d}z - \mathbf{f}_w\right) \tag{22}$$

where the ratio $\frac{\min(h,h_{D,0})}{h}$ accounts for the fact that the dissipation mechanism is exerted over the depth $\min(h, h_{D,0})$, while the momentum source term is applied to the overall water column with height h. Note that The ratio $h/h_{D,0}$ may be interpreted as the inundation ratio Λ.

The second mechanism stems from the drag forces exerted by the obstacle walls onto the fluid. Such drag forces are mainly due to the swirls dissipating energy and the reaction of the obstacle walls onto the water (Figure 4b). Bearing in mind that no satisfactory mathematical model has been proposed so far for this term when the flow is not aligned with the main street axes [23], the drag formula (16c) is retained, with the same proportionality ratio as for the transient source term

$$\mathbf{f}_{D,1} = -\frac{\min(h, h_{D,0})}{h}\int_{\Omega} g\mathbf{C}_{D,1}\,|\mathbf{u}|\,\mathbf{u}\mathrm{d}\Omega \tag{23}$$

The third mechanism is present only when the obstacles are submerged, that is, when the water depth h is larger than the height $h_{D,0}$ of the obstacles (Figure 4c). Submerged obstacles are assumed to act as a "macro-roughness" onto the flow layer flowing above. The additional drag is induced by the friction onto the top of the obstacles and by the disturbances created by the uneven free surface levels and non-uniform depth-averaged velocity field. This additional drag term is activated only if the overtopping flow depth $h - h_{D,0}$ is larger than zero. It is assumed independent of the overflowing depth $h - h_{D,0}$, proportional to the square of the flow velocity as usual turbulent head loss terms, and scaled by a second drag tensor $\mathbf{C}_{D,2}$

$$\mathbf{f}_{D,2} = \begin{cases} -\int_{\Omega} g\mathbf{C}_{D,2}\,|\mathbf{u}|\,\mathbf{u}\mathrm{d}\Omega & \text{if} \quad h > h_{D,0} \\ 0 & \text{if} \quad h \leq h_{D,0} \end{cases} \tag{24}$$

The last two mechanisms bear similarities with the multi-stage behaviour of the friction coefficient identified in [31]. Equations (16a-16e) are replaced with Equations (22-24) and $\mathbf{f}_D = \mathbf{f}_{D,1} + \mathbf{f}_{D,2}$.

2.6 Differential form

The differential form of the equations is obtained by applying the divergence theorem to Equations (6, 7). The integrals in the equation are removed by noticing that the equation holds for all Ω. Incorporating the pressure force $\mathbf{f}_w$ at the water-water interface in the flux tensor, grouping the solid-water force $\mathbf{f}_s$ and the friction term $\mathbf{f}_f$ into the source term gives

$$\partial_t\mathbf{v} + (\mathbf{I} - \mathbf{M})\,\nabla.\mathbf{F} = \mathbf{s} \tag{25a}$$

$$\mathbf{v} = \begin{bmatrix} \theta_\Omega \\ q_\Omega \\ r_\Omega \end{bmatrix}, \quad \mathbf{F} = \begin{bmatrix} q_\Gamma & r_\Gamma \\ \frac{q_\Gamma^2}{\theta_\Gamma} + f_{w,\Gamma} & \frac{q_\Gamma r_\Gamma}{\theta_\Gamma} \\ \frac{q_\Gamma r_\Gamma}{\theta_\Gamma} & \frac{r_\Gamma^2}{\theta_\Gamma} + f_{w,\Gamma} \end{bmatrix}, \quad \mathbf{s} = \begin{bmatrix} 0 \\ \partial_x f_s - g\theta_\Omega s_{f,x} \\ \partial_y f_s - g\theta_\Omega s_{f,y} \end{bmatrix} \tag{25b}$$

$$f_{w,\Gamma} = \int_{z_b}^{z_{s,\Gamma}} \phi_\Gamma(\zeta)\,g\,(z-\zeta)\,\mathrm{d}\zeta \tag{25c}$$

where q and r are respectively the $x-$ and $y-$components of the unit discharge. The non-conservation form follows

$$\partial_t\mathbf{v} + (\mathbf{I} - \mathbf{M})\,\mathbf{A}_x\partial_x\mathbf{v} + (\mathbf{I} - \mathbf{M})\,\mathbf{A}_y\partial_y\mathbf{v} = \mathbf{s} \tag{26a}$$

$$\mathbf{A}_x = \partial_{\mathbf{v}}\mathbf{f}_x, \quad \mathbf{A}_y = \partial_{\mathbf{v}}\mathbf{f}_y \tag{26b}$$

where $\mathbf{f}_x$ and $\mathbf{f}_y$ are respectively the first and second column of the flux tensor $\mathbf{F}$. Straightforward algebra yields the following expressions for the IP and DIP closures (see the details in Appendix A)

$$\mathbf{A}_{x,\mathrm{IP}} = \begin{bmatrix} \left(\frac{\phi_\Gamma}{\phi_\Omega} - \frac{\theta_\Gamma}{\theta_\Omega}\right)u_\Omega & \frac{\theta_\Gamma}{\theta_\Omega} & 0 \\ \left(\frac{\phi_\Gamma}{\phi_\Omega} - 2\frac{\theta_\Gamma}{\theta_\Omega}\right)u_\Omega^2 + \frac{\theta_\Gamma}{\theta_\Omega}c_\Omega^2 & 2\frac{\theta_\Gamma}{\theta_\Omega}u_\Omega & 0 \\ \left(\frac{\phi_\Gamma}{\phi_\Omega} - 2\frac{\theta_\Gamma}{\theta_\Omega}\right)u_\Omega v_\Omega & \frac{\theta_\Gamma}{\theta_\Omega}v_\Omega & \frac{\theta_\Gamma}{\theta_\Omega}u_\Omega \end{bmatrix} \tag{27a}$$

$$\mathbf{A}_{x,\mathrm{DIP}} = \begin{bmatrix} 0 & 1 & 0 \\ \frac{\theta_\Gamma}{\theta_\Omega} c_\Omega^2 - \frac{\phi_\Gamma}{\phi_\Omega}\frac{\theta_\Omega^2}{\theta_\Gamma^2} u_\Omega^2 & 2\frac{\theta_\Omega}{\theta_\Gamma} u_\Omega & 0 \\ -\frac{\phi_\Gamma}{\phi_\Omega}\frac{\theta_\Omega^2}{\theta_\Gamma^2} u_\Omega v_\Omega & \frac{\theta_\Omega}{\theta_\Gamma} v_\Omega & \frac{\theta_\Omega}{\theta_\Gamma} u_\Omega \end{bmatrix} \tag{27b}$$

$$c_\Omega = \left(g \frac{\theta_\Omega}{\phi_\Omega} \right)^{\frac{1}{2}} \tag{27c}$$

The eigenvalues of the matrices are (see Appendix A)

$$\lambda_{\mathrm{IP}}^{(p)} = \frac{1}{2}\left(\frac{\phi_\Gamma}{\phi_\Omega} + \frac{\theta_\Gamma}{\theta_\Omega}\right) u_\Omega + (p-2)\left(\frac{1}{4}\left(\frac{\phi_\Gamma}{\phi_\Omega} - \frac{\theta_\Gamma}{\theta_\Omega}\right) u_\Omega^2 + \left(\frac{\theta_\Gamma}{\theta_\Omega}\right)^2 c_\Omega^2\right)^{\frac{1}{2}}, \quad p = 1, 3 \tag{28a}$$

$$\lambda_{\mathrm{IP}}^{(2)} = \frac{\theta_\Gamma}{\theta_\Omega} u_\Omega \tag{28b}$$

$$\lambda_{\mathrm{DIP}}^{(p)} = \frac{\theta_\Omega}{\theta_\Gamma} u_\Omega + (p-2)\left(\left(\frac{\theta_\Omega}{\theta_\Gamma}\right)^2 \left(1 - \frac{\phi_\Gamma}{\phi_\Omega}\right) u_\Omega^2 + \frac{\theta_\Gamma}{\theta_\Omega} c_\Omega^2\right)^{1/2}, \quad p = 1, 2, 3 \tag{28c}$$

These formulae are generalizations of the wave speed formulae given in [24]. Assume indeed that both ϕ_Ω and ϕ_Γ are independent of z. Then, $\frac{\phi_\Gamma}{\phi_\Omega} = \frac{\theta_\Gamma}{\theta_\Omega}$ and the above equations simplify to

$$\lambda_{\mathrm{IP}}^{(p)} = \frac{\phi_\Gamma}{\phi_\Omega}\left(u_\Omega + (p-2)\, c_\Omega\right), \quad p = 1, 2, 3 \tag{29a}$$

$$\lambda_{\mathrm{DIP}}^{(p)} = \frac{\phi_\Gamma}{\phi_\Omega} u_\Omega + (p-2)\left(\frac{\phi_\Omega}{\phi_\Gamma}\left(\frac{\phi_\Omega}{\phi_\Gamma} - 1\right) u_\Omega^2 + \frac{\phi_\Gamma}{\phi_\Omega} c_\Omega^2\right)^{1/2}, \quad p = 1, 2, 3 \tag{29b}$$

that are the wave speed formulae derived in [24]. Another simplification arises when $\phi_\Gamma(z) = \phi_\Omega(z)\, \forall z$. Then,

$$\lambda_{\mathrm{IP}}^{(p)} = \lambda_{\mathrm{DIP}}^{(p)} = u_\Omega + (p-2)\, c_\Omega, \quad p = 1, 2, 3 \tag{30}$$

and the wave propagation speeds of the SP equations are obtained.

3 Numerical aspects

3.1 Finite volume discretization

The governing equations are discretized using an unstructured finite volume grid. A first-order time splitting procedure [43, 45] is used, with the following solution sequence [24]

$$\mathbf{v}_i^{n+1} = \mathbf{SMH}\mathbf{v}_i^n \tag{31}$$

where $\mathbf{v}_i^n$ is the averaged variable vector over the computational cell i at the time level n, $\mathbf{H}$, $\mathbf{M}$ and $\mathbf{S}$ are respectively the hyperbolic operator, the momentum dissipation tensor in Equations (16d, 16e) and the friction/building drag operator. The application of the momentum dissipation operator $\mathbf{M}$ is straightforward. The bottom and drag source term operator uses an unconditionally stable, linearised approach presented in [24] and are not detailed here.

The terms accounted for by the operator $\mathbf{H}$ are the mass and momentum fluxes, as well as the geometric source term $\mathbf{f}_s$ under the form (14):

$$\mathbf{H}\mathbf{v}_i^n = \frac{\Delta t}{A_i} \sum_{j \in N(i)} W_{ij} \mathbf{F}_{ij} \mathbf{n}_{ij} + (\mathbf{f}_s)_{ij,i} \tag{32}$$

where A_i is the plan view area of the computational cell i, $N(i)$ is the set of neighbour cells of the cell i, the subscript ij denotes the interface between the cells i and j, W_{ij}, $\mathbf{F}_{ij}$ and $\mathbf{n}_{ij}$ are respectively the width, the flux tensor and the normal unit vector for the interface ij. $(\mathbf{f}_s)_{ij,i}$ is the part of the geometric source term $\mathbf{f}_s$ distributed to the cell i in the momentum balance process. The flux tensor and the source term are computed in a local coordinate system attached to the interface. In such a coordinate

system, the problem is one-dimensional with respect to the normal direction to the interface. The flux $\mathbf{F}_{ij}$ is computed as the solution of a Riemann problem. The approximate HLLC formulation [46] is used. The following flux formulae are obtained (see Appendix B for a detailed derivation)

$$q_{ij} = \frac{\phi_{\Gamma,R}\lambda^+ q_L - \phi_{\Gamma,L}\lambda^- q_R}{\phi_{\Gamma,R}\lambda^+ - \phi_{\Gamma,L}\lambda^-} - \frac{\phi_{\Gamma,L}\lambda^-\phi_{\Gamma,R}\lambda^+}{\phi_{\Gamma,R}\lambda^+ - \phi_{\Gamma,L}\lambda^-}\left(z_{s,\Gamma,L} - z_{s,\Gamma,R}\right) \tag{33a}$$

$$M_{ij} = \frac{\lambda^+ M_L - \lambda^- M_R}{\lambda^+ - \lambda^-} - \frac{\lambda^+\lambda^-}{\lambda^+ - \lambda^-}\left(q_L - q_R\right) \tag{33b}$$

$$\left(qv\right)_{ij} = \frac{q_{ij} + |q_{ij}|}{2} v_L + \frac{q_{ij} - |q_{ij}|}{2} v_R \tag{33c}$$

$$\phi_{\Gamma,S} = \phi_{\Gamma,ij}\left(z_{s,\Gamma,S}\right), \quad S = L, R \tag{33d}$$

where the subscripts L and R denote the left and right states of the Riemann problem. The speeds $\lambda^\pm$ are computed using Davis's wave speed estimates [12]. Equations (33a, 33b) are obtained from the HLL relationships, while Equation (33c) stems from the contact surface restoration method [46] that contributes to minimize numerical diffusion. In the numerical implementation of the method, both the first-order, Godunov approach [19] and the MUSCL-EVR reconstruction [41] are implemented. Note that formulae (33a-33d) fulfil the so-called C-property [3]

$$\left.\begin{array}{c}\left(z_{s,\Gamma}\right)_L = \left(z_{s,\Gamma}\right)_R \\ q_L = q_R = 0\end{array}\right\} \Rightarrow \left\{\begin{array}{c} q_{ij} = 0 \\ M_{ij} = M_L = M_R\end{array}\right. \tag{34}$$

that is, the preservation of equilibrium states.

3.2 Porosity law discretization

The laws $\phi_D\left(z\right)\left(D = \Omega, \Gamma\right)$ are discretized with an arbitrary level of accuracy as follows. Assume that the law $\phi\left(z\right)$ is known (the subscript D is dropped for the sake of readability). A sample law is illustrated by the dashed line on Figure 5a. Integrating ϕ with respect to z yields the law $\theta\left(z\right)$ (solid line on Figure 5b). The law $\theta\left(z\right)$ is tabulated using N points $\left(z_i^{\text{tab}}, \theta_i^{\text{tab}}\right), i = 1, \ldots, N$ (Figure 5b). The tabulated values for θ are defined so as to preserve mass conservation, $\theta_i^{\text{tab}} = \theta\left(z_i^{\text{tab}}\right)$. Approximating the tabulated θ function with a piecewise linear law, using $z = \partial_z\theta$ gives:

$$\theta^{\text{tab}}\left(z\right) = \left\{\begin{array}{ccc} 0 & \text{if} & z < z_1^{\text{tab}} \\ \theta_i^{\text{tab}} + \frac{\theta_{i+1}^{\text{tab}} - \theta_i^{\text{tab}}}{z_{i+1}^{\text{tab}} - z_i^{\text{tab}}}\left(z - z_i^{\text{tab}}\right) & \text{if} & z_i^{\text{tab}} \le z < z_{i+1}^{\text{tab}} \\ \theta_N^{\text{tab}} & \text{if} & z_N^{\text{tab}} \le z \end{array}\right. \tag{35a}$$

$$\phi^{\text{tab}}\left(z\right) = \left\{\begin{array}{ccc} 0 & \text{if} & z < z_1^{\text{tab}} \\ \phi_i^{\text{tab}} = \frac{\theta_{i+1}^{\text{tab}} - \theta_i^{\text{tab}}}{z_{i+1}^{\text{tab}} - z_i^{\text{tab}}} & \text{if} & z_i^{\text{tab}} \le z < z_{i+1}^{\text{tab}} \\ \phi_N^{\text{tab}} = \phi\left(z_N^{\text{tab}}\right) & \text{if} & z_N^{\text{tab}} \le z \end{array}\right. \tag{35b}$$

The tabulated porosity law $\phi^{\text{tab}(z)}$ is thus piecewise constant, as shown on Figure 5a (bold line). The tabulated value ϕ_i^{tab} is equal to the average value of the exact function $\phi\left(z\right)$ over the interval $\left[z_i^{\text{tab}}, z_{i+1}^{\text{tab}}\right]$. This approach has the advantage that the tabulated law $\theta^{\text{tab}}\left(z\right)$ is exact for the N values of $z{=}\mathrm{z}_i^{\text{tab}}$. The accuracy of the tabulated laws is limited only by the number N of discretization levels. Compared to previously presented approaches [49, 35, 34], the accuracy of the discretization can be adapted to the complexity of the geometry. Moreover, non-monotone $\phi\left(z\right)$ functions can be defined.

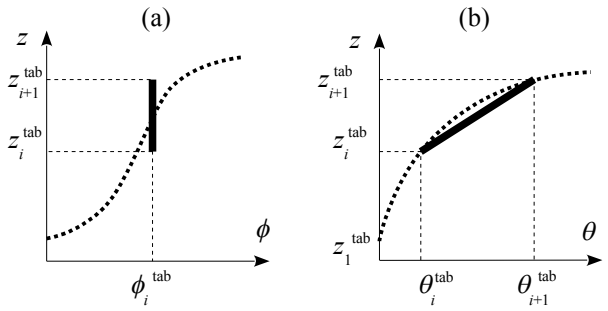

Figure 5: Tabulated porosity laws. Definition sketch. a: exact $\phi(z)$ law (dashed line) and discretized law $\phi^{\text{tab}}(z)$ (bold line). b: $\theta(z)$ law inferred from $\phi(z)$ and sampling points $\left(\theta_i^{\text{tab}}, z_i^{\text{tab}}\right)$.

The influence of the number N of tabulation entries is illustrated by Figure 6. A hypothetical, piecewise linear law $\phi(z)$ is generated using a random distribution for 28 couples (z, ϕ) (dots on Figure 6, left) and connecting these points with straight lines. The resulting $\phi^{\text{tab}}(z)$ law is illustrated by the solid line on the (ϕ, z) graph. The corresponding exact law $\theta(z)$ and the tabulated law $\theta^{\text{tab}}(z)$ are shown on Figure 6, right-hand side (θ, z) graphs. The following values are used for N: $N = 5$ (Figure 6, top), $N = 9$ (Figure 6, middle) and $N = 15$ (Figure 6, bottom). While $N = 5$ yields a crude approximation of the "true" law $\phi(z)$, it allows for a fairly accurate discretization of the law $\theta(z)$, except in the neighbourhood of the inflection point of ϕ. With $N = 9$, the law $\theta(z)$ is approximated with satisfactory accuracy, while the tabulated porosity law $\phi^{\text{tab}}(z)$ is inaccurate only in the central part of the discretization interval. $N = 15$ yields a very good approximation for both ϕ and θ. For practical applications, $5 \leq N \leq 10$ might appear as a satisfactory trade-off between computational efficiency and accuracy. This point is illustrated by test cases presented in Section 4.

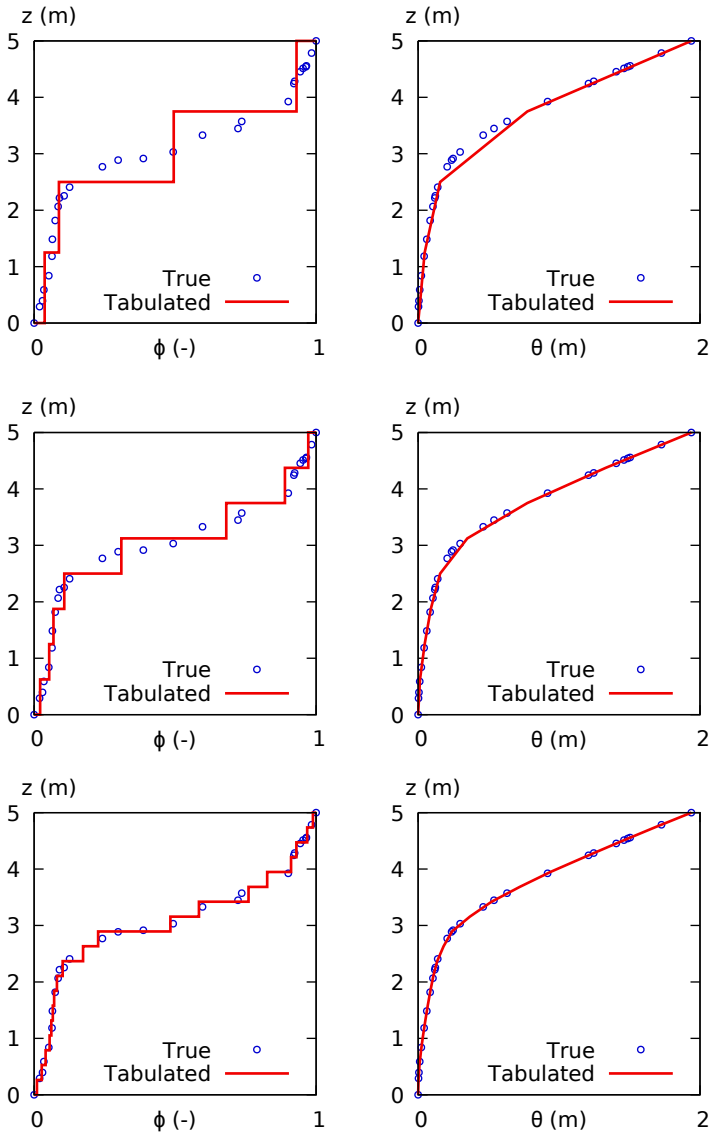

Figure 6: Sample tabulated porosity laws. Top: $N = 5$. Middle: $N = 9$. Bottom: $N = 15$.

4 Computational examples

4.1 Test 1: dambreak problem in a triangular valley

The purpose of this test is to assess the influence of the tabulated porosity laws on the accuracy of the computational solution. The Riemann, initial value problem is solved for a triangular cross-section (Figure 7). The storage and conveyance porosities are identical, linear functions of the elevation

$$\phi_\Omega(z) = \phi_\Gamma(z) = \frac{\tan\alpha}{2}\frac{z}{z_{\max}} = \phi_{\max}\frac{z}{z_{\max}} \tag{36a}$$

$$z_s(x,0) = \begin{cases} z_L & \text{if} \quad x < x_0 \\ z_R & \text{if} \quad x > x_0 \end{cases} \tag{36b}$$

The analytical solution is made of a region of constant state connected to the left and right states by a rarefaction wave and a shock respectively. The water depth h_* and the flow velocity u_* in the intermediate region of constant state satisfy the following 3×3 non-linear system:

$$u_* + 4c_* = 4c_L \tag{37a}$$

$$\left(h^2 u\right)_* = \left(h_*^2 - h_R^2\right) s \tag{37b}$$

$$\left(\frac{h^2 u^2}{2} + \frac{g}{6} h^3\right)_* - \frac{g}{6} h_R^3 = \left(\frac{h^2 u}{2}\right)_* s \tag{37c}$$

where $c = (gh/2)^{1/2}$ is the propagation speed of waves in still water for a triangular channel and s is the speed of the shock wave.

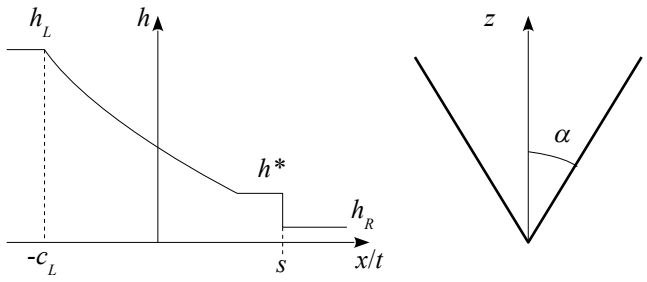

Figure 7: Test 1: dambreak in a triangular valley. Definition sketch.

Equation (37a) stems directly from the Riemann invariant $u + 4c$ across the wave $\mathrm{d}x/\mathrm{d}t = u + c$ [20]. Equations (37b-37c) are the Rankine-Hugoniot conditions for mass and momentum respectively. Solving the above system for (h_*, u_*, s) yields the solution

$$h(x,t) = \begin{cases} h_L & \text{if} \quad -\frac{x}{t} \leq -c_L \\ \frac{2c^2(x/t)}{g} & \text{if} \quad -c_L \leq \frac{x}{t} < u_* - c_* \\ h_* & \text{if} \quad u_* - c_* \leq \frac{x}{t} < s \\ h_R & \text{if} \quad s < \frac{x}{t} \end{cases} \tag{38a}$$

$$u(x,t) = \begin{cases} 0 & \text{if} \quad -\frac{x}{t} \leq -c_L \\ \frac{4}{5}\left(c_L + \frac{x}{t}\right) & \text{if} \quad -c_L \leq \frac{x}{t} < u_* - c_* \\ u_* & \text{if} \quad u_* - c_* \leq \frac{x}{t} < s \\ 0 & \text{if} \quad s < \frac{x}{t} \end{cases} \tag{38b}$$

$$c\left(\frac{x}{t}\right) = \frac{1}{5}\left(4c_L - \frac{x}{t}\right) \tag{38c}$$

Since the functions $\phi_\Gamma(z)$ and $\phi_\Omega(z)$ are identical, the IP and DIP closures give identically $\mathbf{u}_\Gamma = \mathbf{u}_\Omega$, thus yielding the same numerical results. The solution is shown on Figure 8 for the parameter set in Table 1. Three different levels of accuracy are tested. For $N = 5$, 10 and 20, the discretization levels z_i^{tab} are set every 2m, 1m and 0.5m respectively.

Parameter	Meaning	Numerical value
g	Gravitational acceleration	$9.81\,\mathrm{m\,s^{-2}}$
h_L	Upstream water depth	10 m
h_R	Downstream water depth	0.5 m
N	Number of tabulation levels	5, 10, 20
t	Simulated time	10 s
$z_{\max}$	Maximum water depth	10 m
$\phi_{\max}$	Maximum porosity value	1

Table 1: Test 1: dambreak in a triangular valley. Parameter set.

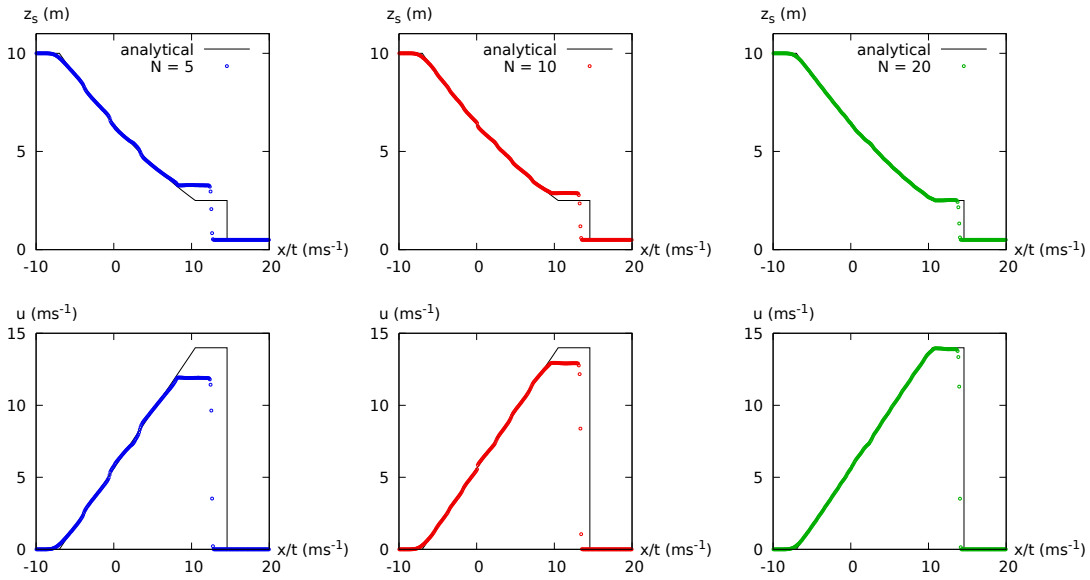

Figure 8: Test 1: dambreak in a triangular valley. Simulation results.

The influence of N is clearly visible on Figure 8. For $N = 5$, the water depth and velocity profiles in the rarefaction wave clearly exhibit sudden slope variations as the free surface elevation profile crosses the tabulated levels z_i^{tab}. While the analytical solution is smooth, the strong porosity variations across the tabulated water levels induce strong variations in the derivatives of the flux functions, hence the slope breaks observed in the numerical profiles. For $N = 10$, the numerical profile becomes smoother and closer to the analytical solution. For $N = 20$, the numerical water depth and velocity profiles are smooth and in very good agreement with the analytical solution. The reader's attention is drawn to the accuracy of the numerical solution in the intermediate region of constant state. For $N = 5$ and $N = 10$, the water depth is significantly overestimated compared to the analytical one. This could be expected because, with the parameters in Table 1, $h_* = 2.505$m. For $N = 5$, the shock is captured by only two tabulated levels. For $N = 10$, only 3 tabulation levels are used to span the range [0m , 2.5m]. With $N = 20$, there is a tabulation level every 50 cm, and h_* is captured by 6 tabulation levels. Therefore, the storage function $\theta(z)$ and the pressure function $f_{w,\Gamma}$ are significantly better described with $N = 20$ than with $N = 5$ or $N = 10$, hence a more accurate estimation of the shock speed. It should also be noted that, for $N = 20$, the location of the numerical shock is wrong by approximately 4 computational cells. However, with $h_* \approx h_L/4$ and the triangular shape of the channel, $\theta(h_*) \approx \theta(h_L)/16$ and the error in the location of the shock is equivalent to an error of less than $1/4$ cell in the initial location of the discontinuity.

4.2 Test 2: dambreak in a compound channel

The purpose is to assess the validity of the depth-dependent porosity approach to model transients in the presence of two-dimensional flow patterns. A frictionless dambreak problem is simulated in a compound channel comprising a rectangular main channel of width W_1 and depth h_0 and a flood plain of width W_2 (Figure 9). The parameters of the test case are given in Table 2. This configuration is similar to that presented in [49], with the difference that no transient analysis is reported in [49]. Two different values are considered for the downstream water level z_R. In the first configuration (Test 2a), z_R =0.5 m is four times as small as the height of the main channel. This is expected to trigger strongly two-dimensional flow patterns in the vicinity of the advancing front, with water spilling from the floodplain into the main channel. In the second configuration (Test 2b), $z_B = 2.5$ m is above the floodplain, which is expected to yield milder flow patterns.

Parameter	Meaning	Numerical value
g	Gravitational acceleration	$9.81\mathrm{m\,s^{-2}}$
h_0	Main channel depth	2 m
h_L	Upstream water depth	10 m
h_R	Downstream water depth	0.5 m (Test 2a), 2.5 m (Test2b)
L	Domain length	2000 m
N	Number of tabulation levels	1
W_1	Main channel width	50 m
W_2	Floodplain width	200 m

Table 2: Test 2: dambreak in a compound channel. Parameter set.

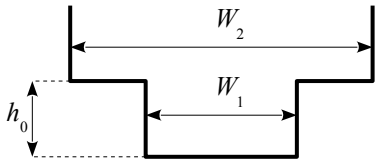

Figure 9: Test 2: dambreak in a compound channel. Geometry definition sketch.

The breaking of the dam is first simulated over 50 seconds by solving the two-dimensional shallow water equations over a 2.5m × 2.5m square grid using the second-order MUSCL-EVR scheme [41]. Since only half of the channel is meshed from symmetry considerations, the computational mesh counts 16,000 cells. Figure 10 shows the simulated free surface at $t = 50$s. The difference between the speeds of the advancing fronts in the main channel and over the floodplain is clearly visible.

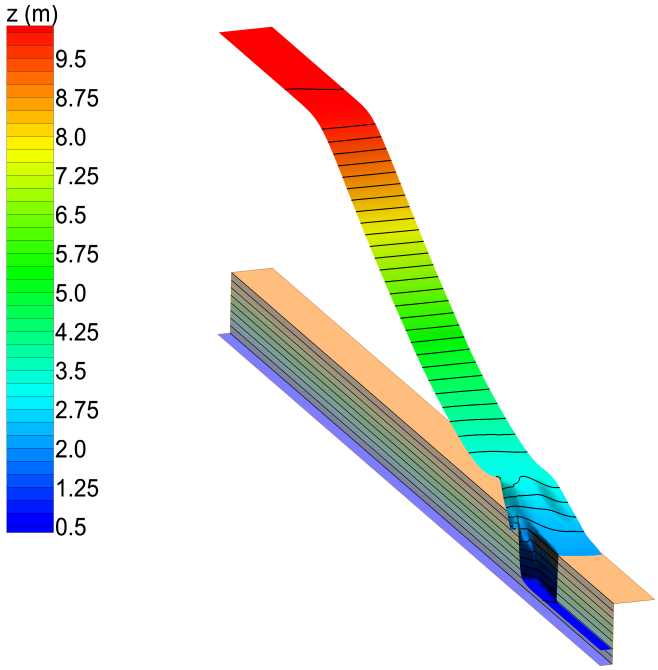

Figure 10: Test 2: dambreak in a compound channel. Bird's eye view of the free surface computed by the 2D shallow water equations at t =50s for Test 2a. $z-$mag 50.

The dambreak is also simulated using the DDP model. The cross-sectional area of the model is represented using a single cell, while the cell spacing in the longitudinal direction is 20 m. The model thus counts only 100 cells. The geometry of the cross-section is represented using a piecewise constant

porosity law:

$$\phi_\Gamma(z) = \phi_\Omega(z) = \begin{cases} \frac{W_1}{W_2} & \text{if} \quad 0 < z < h_0 \\ 1 & \text{if} \quad z > h_0 \end{cases} \tag{39}$$

With $N = 2$ the discretization (35a, 35b) is exact. As in the previous test case, the IP and DIP closures yield identical results. Figures 11 and 12 show respectively the results for Test 2a and Test 2b. All profiles are represented as functions of the x/t coordinate. The results of the two-dimensional shallow water model are averaged over the coarse grid of the DDP model, a standard procedure for refined model and porosity model comparison [29].

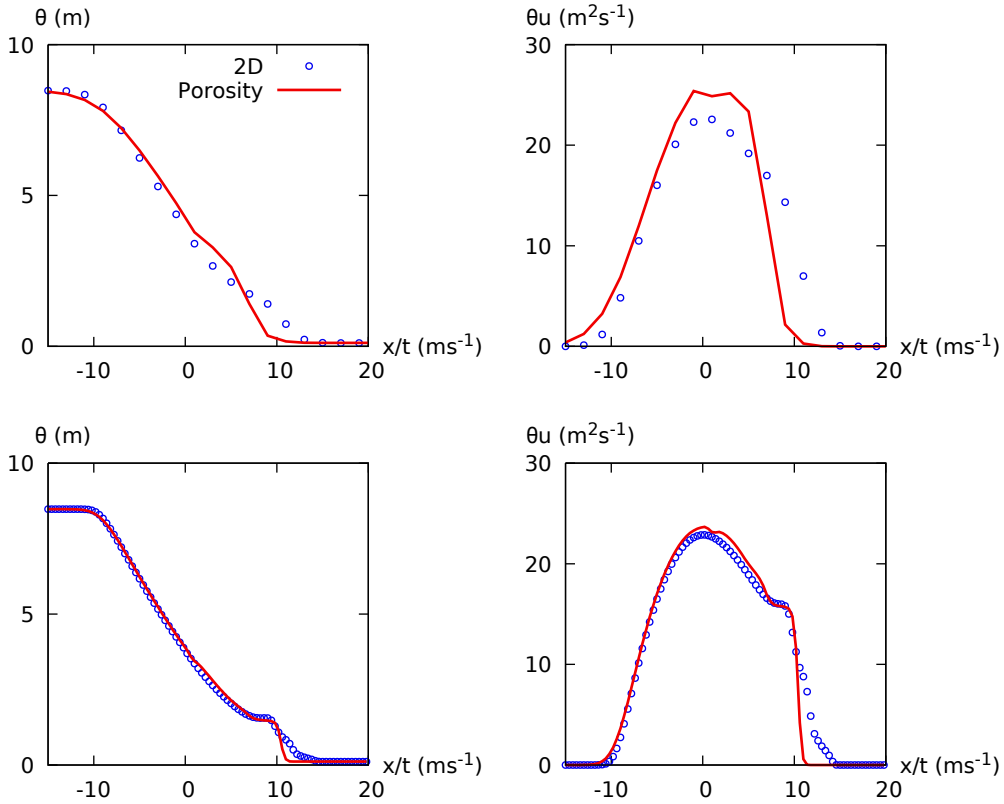

Figure 11: Test 2: dambreak in a compound channel. Simulation results for Test 2a ($h_R = 0.5$m). Free surface and unit discharge profiles at $t = 10$s (top) and $t = 50$s (bottom). Dots: free surface elevations and unit discharges computed by the 2D shallow water model, averaged over the computational grid of the DDP model. Solid line: DDP model solution.

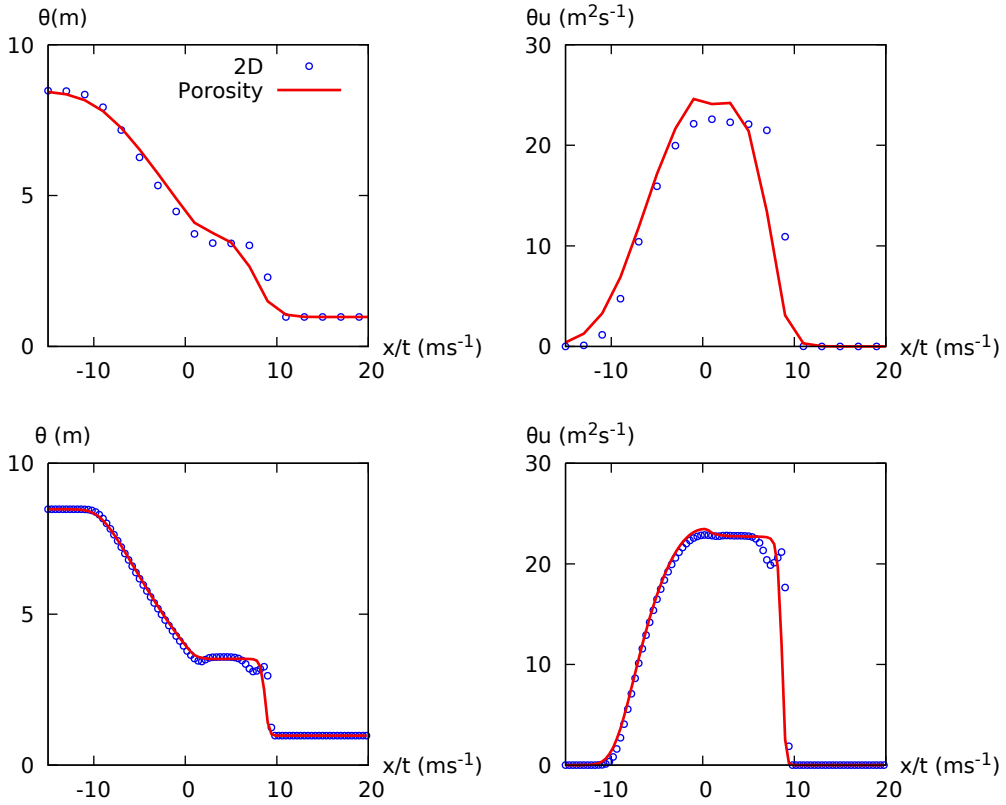

Figure 12: Test 2: dambreak in a compound channel. Simulation results for Test 2b ($h_R = 2.5$m). Free surface and unit discharge profiles at $t = 10$s (top) and $t = 50$s (bottom). Dots: free surface elevations and unit discharges computed by the 2D shallow water model, averaged over the computational grid of the DDP model. Solid line: DDP model solution.

Overall, the DDP model provides a satisfactory, large scale description of the free surface and unit discharge profiles obtained from the shallow water model. For Test 2a, however, the DDP model underestimates the smearing of the shock in the averaged 2D solution. The ratio of the 2D to DDP shock width is between 2 and 3. This is identically true for $t = 10$s (Figure 11, top) and $t = 50$s (Figure 11, bottom). The reason for shock smearing is easy to identify: the shock travels at different speeds in the main channel and the floodplain. Part of the water in the floodplain spills into the main channel, as can be seen on Figure 10. As a result, the free surface in the floodplain exhibits a milder shock profile than it would if there was no exchange with the main channel. This interpretation is confirmed by the examination of Test 2b (Figure 12). In this configuration, owing to the higher downstream water level ($z_R = 2.5$m), the exchange between the floodplain and the main channel is limited and the shock remains sharper.

4.3 Test 3: urban dambreak problem

The purpose of this test, originally proposed in [21], is to investigate the accuracy of the domain-boundary closure models. It has been used to check the validity of the SP, IP and DIP closures (17a-19b) in a number of publications [21, 22, 23, 24, 35]. It has also been used to validate the transient momentum dissipation term embedded in the DIP model [23, 24]. The IP closure has been reported to yield underestimated wave propagation speeds with respect to those of the refined flow solutions [21, 24, 35]. The DIP closure allows the accuracy of the porosity model solution to be improved to a large extent [23, 24]. However, in all the abovementioned references, the urban dambreak problem has been applied using depth-independent porosity functions. Even in the depth-dependent integral porosity model proposed in [35], the building blocks in the simulation are made taller than the maximum water depth. This does not allow the closure to be tested over the full range of possible flow configurations. For this reason, the present urban dambreak problem involves flow configurations where

the buildings are submerged by the water wave, at least over part of the domain. This configuration also allows the proposed momentum source term models to be tested and their relevance to be assessed.

The geometry is illustrated by Figure 13 (Table 3). An idealized neighbourhood made of equally spaced, square buildings is generated. The street width and building width are taken identical, equal to $l/2$, where l is the spatial period. The height of the buildings is $h_{D,0}$. The bottom is horizontal, friction is neglected. The water depths on the left- and right-hand sides of the dam are denoted by h_L and h_R respectively (Table 4). Using symmetry considerations, only half a period is meshed in the transverse direction. The refined 2D shallow water model uses 1m×1m square cells, for a total 20,000 cells in the model. In contrast, the DDP model uses $20\text{m} \times 20\text{m}$ cells, with the following depth-dependent porosity laws:

$$\phi_\Omega(z) = \begin{cases} \frac{3}{4} & \text{if} \quad z < h_{D,0} \\ 1 & \text{if} \quad z > h_{D,0} \end{cases} \tag{40a}$$

$$\phi_\Gamma(z) = \begin{cases} \frac{1}{2} & \text{if} \quad z < h_{D,0} \\ 1 & \text{if} \quad z > h_{D,0} \end{cases} \tag{40b}$$

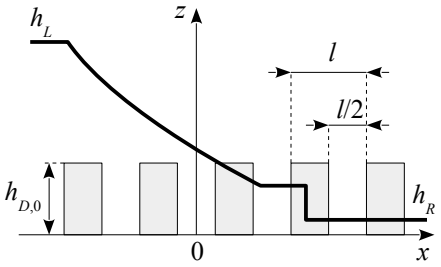

Figure 13: Test 3: urban dambreak problem. Definition sketch.

Parameter	Meaning	Numerical value
g	Gravitational acceleration	$9.81\text{m}\,\text{s}^{-2}$
$h_{D,0}$	Building height	5 m
L	Domain length	2000 m
l	Spatial period	20 m
N	Number of tabulation levels for $\phi_\Omega(z)$ and $\phi_\Gamma(z)$	1
W	Domain width	20 m

Table 3: Test 3: urban dambreak problem. Geometric parameters.

Test	h_L	h_R
3a	10 m	0.1 m
3b	10 m	2 m
3c	5 m	0.1 m
3d	5 m	2 m

Table 4: Test 3: urban dambreak problem. Configuration nomenclature.

Since the laws $\phi_\Gamma(z)$ and $\phi_\Omega(z)$ are different, the IP and DIP closures give different numerical results. Figure 14 provides a comparison between the refined two-dimensional model results and those given by the DDP model. The results of the 2D model are averaged over the computational grid of the DDP model [29]. The transient source term (16d, 16e) in the DDP model is calibrated so as to achieve the best trade-off between shock speed and post-shock water depths. Since the flow is parallel to the $x-$axis, $\mu_y = \mu_{yy} = 0$ and only μ_{xx} is to be calibrated. The calibrated values are given in Table 5. Note that the building height $h_{D,0}$ is used in Equation (24) without calibration.

Test	μ_{xx} IP closure	$C_{D,2}$ IP closure	μ_{xx} DIP closure	$C_{D,2}$ DIP closure
3a	0.	10^{-2}	0.27	9×10^{-3}
3b	0.	8×10^{-3}	0.25	4.5×10^{-3}
3c	0.	5×10^{-3}	0.30	0.
3d	0.	0.	0.25	0.

Table 5: Test 3: urban dambreak problem. Calibrated momentum dissipation parameters.

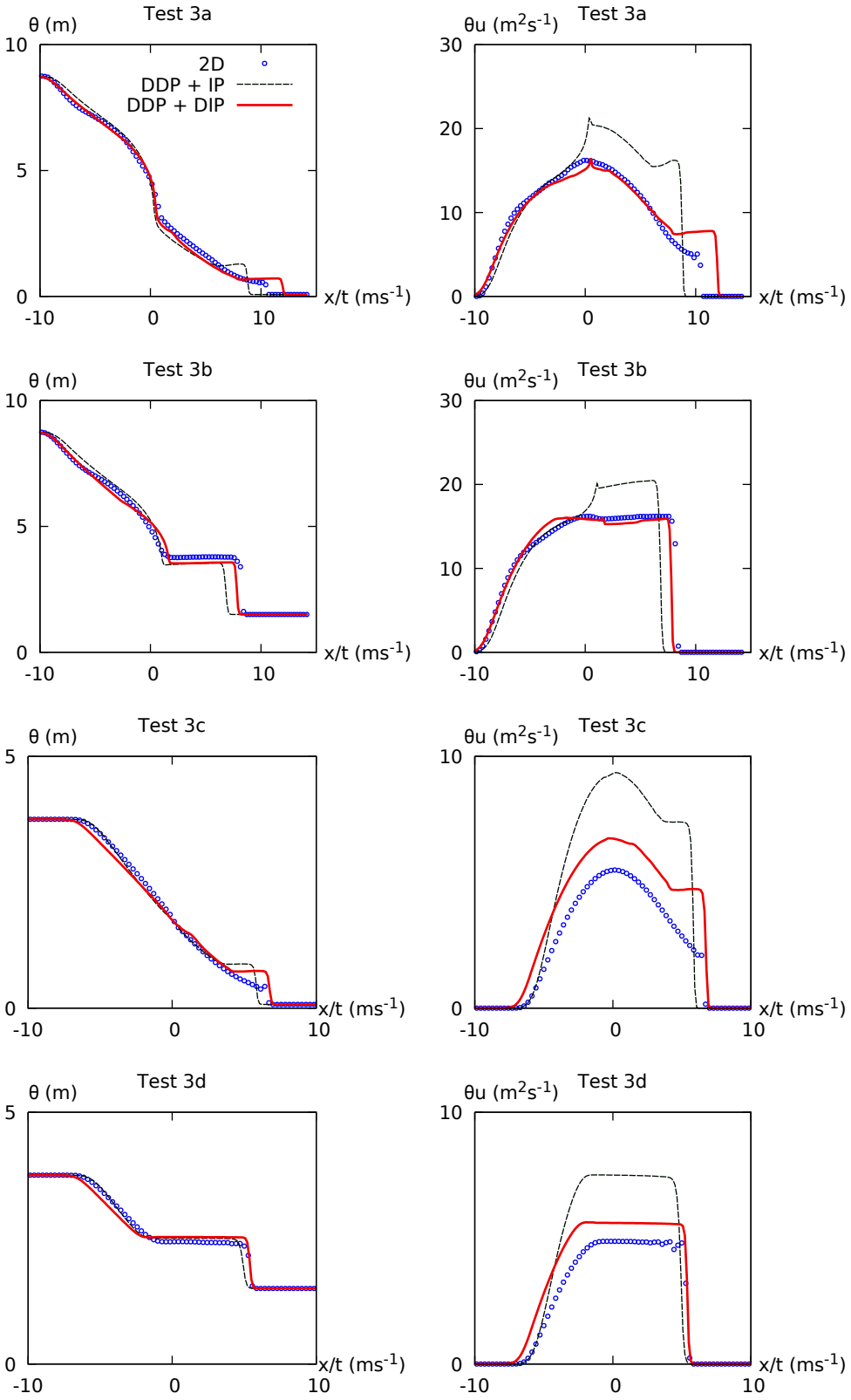

Figure 14: Test 3: urban dambreak problem. Simulation results at $t = 70$s. Dots: water depths and unit discharges computed by the 2D shallow water model, averaged over the computational grid of the DDP model. Solid lines: DDP model solutions.

The following conclusions can be drawn. First, the IP closure consistently yields underestimated shock speeds, overestimated water depths behind the shock and overestimated unit discharge profiles. For this reason, μ_{xx} is consistently set to zero for this closure because a non-zero μ_{xx} would increase the post-shock water depth and reduce the shock speed even further. This feature of the IP closure was already known from test involving depth-independent porosity fields [24]. Second, the DIP closure yields significantly improved water depths and unit discharge profiles compared to the IP closure. However, while the average water depth profiles can be reconstructed with a satisfactory accuracy, the unit discharge profiles are overestimated by approximately 20% (against more than 50% with the IP closure). It must be noted however that in Tests 3c-d, the DIP model provides less accurate unit discharge profiles than in Tests 3a-b. Since the depth-dependent drag term is active in Tests 3a-b and inactive in Tests 3c-d, it may be argued that the transient source term model is inefficient and that the better agreement obtained with Tests 3a-b is only due to the activation of the depth-dependent drag term, that provides an additional degree of freedom for model calibration.

To answer this question, a sensitivity analysis to the structure of the model is carried out. Figure 15 shows the water depths and unit discharge profiles obtained for Test 3a in the following four configurations. The profiles on Figure 15a-b are obtained by setting $C_{D,2} = \mu_{xx} = 0$. With this parameter combination, the speed of the shock is overestimated by a factor 3. The unit discharge profile is also overestimated by approximately 25%. Moreover, the DDP model fails to replicate the concavity of the water depth profile for $-5 \leq \frac{x}{t} \leq 0$ and the breaking slope in the unit discharge profile in the rarefaction wave. Activating the transient momentum source term while keeping the drag coefficient $C_{D,2} = 0$ leads to the profiles shown on Figures 15c-d. The best compromise between shock location and post-shock water depth is obtained for $\mu_{xx} = 0.27$. While the transient source term allows for a better reconstruction of the shock, the model again fails to replicate the concavity in the water depth profile and the slope break in the unit discharge profile. The profiles on Figure 15e-f are obtained by setting $\mu_{xx} = 0$ and calibrating $C_{D,2} = 9 \times 10^{-3}$. The free surface and unit discharge profiles are better replicated over the entire rarefaction wave, but the speed of the shock is again overestimated by a factor approximately equal to 3. Only using non-zero drag coefficient and momentum dissipation terms$(C_{D,2}, \mu_{xx}) = \left(7 \times 10^{-3}, 0.25\right)$ allows correct profiles to be obtained in both the rarefaction wave and behind the shock (Figure 15g-h). None of the two models alone allows correct profiles to be obtained and the two source term models must be combined in order to reconstruct the refined model solution accurately. Lastly, the relevance of the threshold $h_{D,0}$ in Equation (24) is checked. Figures 15i-j show the optimal profiles obtained by setting $h_{D,0} = 0$ in the equation. In other words, the drag term is applied at all points, regardless of the respective positions of the free surface and the top of the obstacles. With the optimal value $C_{D,2} = 5 \times 10^{-3}$, the model successfully reproduces the maximum value of the unit discharge profile and a correct shock location. However, as far as the water depth profile is concerned, the variations in the curvature of the profile is not reproduced accurately. Concerning the unit discharge profile, the slope break in the upstream part of the rarefaction wave is missed. The unit discharge is consistently underestimated in the downstream part of the profile.

As a conclusion of this sensitivity analysis, only the combination of the transient source term model (22) and the threshold-based drag model (24) allows accurate solutions to be achieved. Dropping any of the features of these two models yields substantial errors in the solutions.

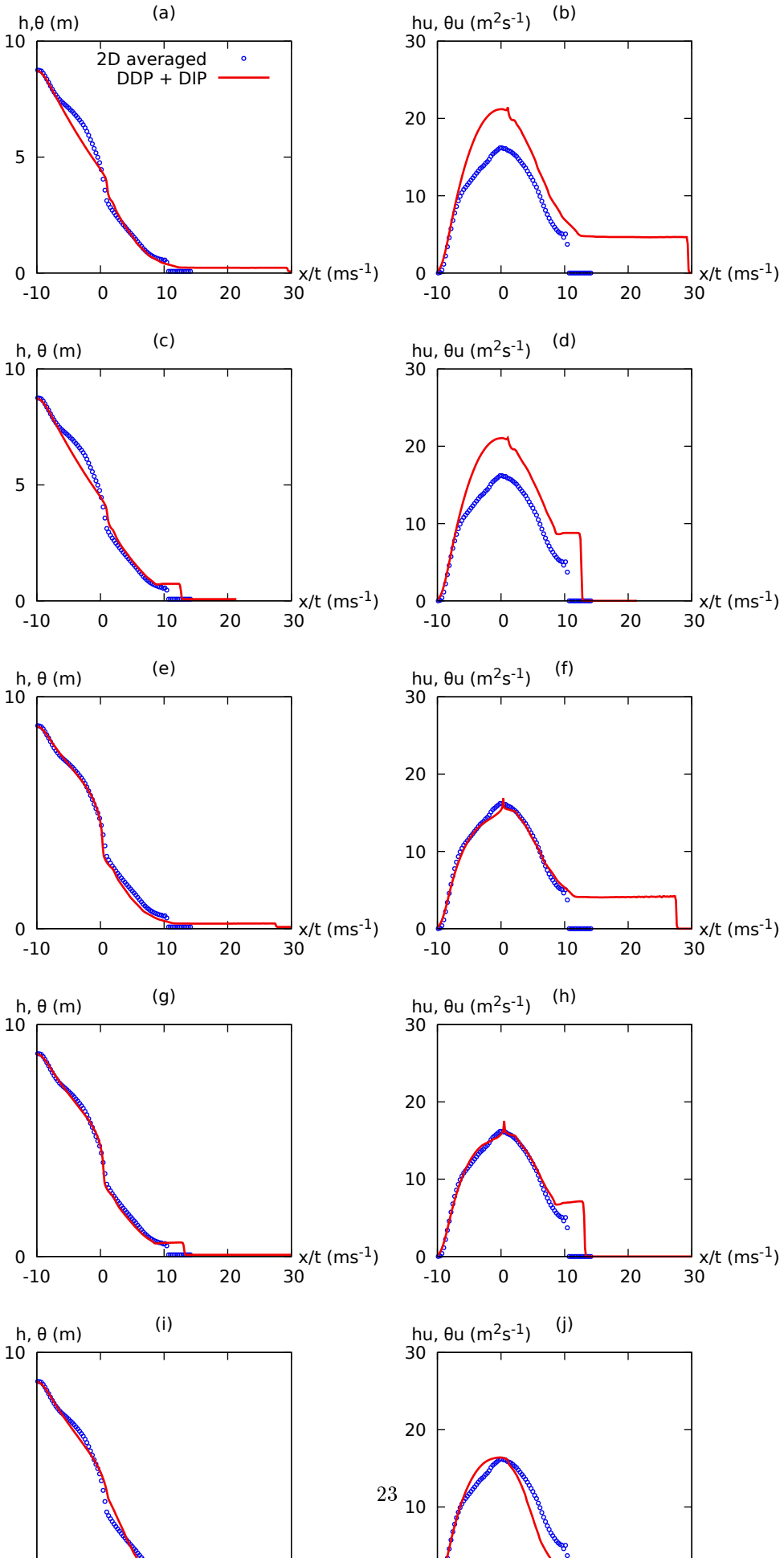
(a)
h,θ (m)
2D averaged
DDP + DIP
x/t (ms-1)
(b)
hu, θu (m2s-1)
x/t (ms-1)
(c)
h, θ (m)
x/t (ms-1)
(d)
hu, θu (m2s-1)
x/t (ms-1)
(e)
h, θ (m)
x/t (ms-1)
(f)
hu, θu (m2s-1)
x/t (ms-1)
(g)
h, θ (m)
x/t (ms-1)
(h)
hu, θu (m2s-1)
x/t (ms-1)
(i)
h, θ (m)
(j)
hu, θu (m2s-1)

4.4 Test 4: dambreak over microtopography

Test 4 consists in simulating the propagation of a dambreak wave over a highly irregular, periodic topography. The objectives of this test are (i) to check the accuracy and stability of the solution obtained with the modified DIP closure in the presence of drying bottoms, (ii) to assess the accuracy of the storage and connectivity porosities as statistical descriptors of the microscale topography. This test is adapted from that originally presented in [34]. While the test presented in [34] uses a sinusoidal topography, the bottom geometry used in the present test follows an asymmetric sawtooth profile with height h_0 and wavelength l (Figure 16, Table 6). This test is instrumental in assessing the ability of the DDP model to model flows over series of furrows, as in the single, depth-dependent porosity model used in [48].

Two different bottom level functions are defined:

$$z_{b,1}(x) = \mod\left(\frac{x}{l}, 1\right) h_0 \tag{41a}$$

$$z_{b,2}(x) = \mod\left(-\frac{x}{l}, 1\right) h_0 \tag{41b}$$

With function $z_{b,1}$ the sawtooth discontinuity faces the direction of positive x, while it faces the direction of negative x with function $z_{b,2}$. These two bottom profiles are described by the same depth-dependent porosity functions:

$$\phi_\Omega(z) = \max\left(0, \min\left(1, \frac{z}{h_0}\right)\right) = \begin{cases} 0 & \text{for} \quad z \leq 0 \\ \frac{z}{h_0} & \text{for} \quad 0 \leq z \leq h_0 \\ 1 & \text{for} \quad z \geq h_0 \end{cases} \tag{42a}$$

$$\phi_\Gamma(z) = H(z - h_0) = \begin{cases} 0 & \text{for} \quad z \leq h_0 \\ 1 & \text{for} \quad z > h_0 \end{cases} \tag{42b}$$

where $H()$ is Heaviside's step function.

Symbol	Parameter	Numerical value
h_0	Microtopography height	0.05 m
L	Domain length	20 m
l	Microtopography wave length	0.5 m
T	simulated time	5 s
W	Domain width	0.5 m

Table 6: Test 4: dambreak over microtopography. Simulation parameters.

The initial conditions are given by Equation (36b). Four configurations are tested (see Table 7). In configurations 4a and 4c the combination (z_L, z_R) is such that the flow remains subcritical at all points. In configurations 4b and 4d, the water level on the right-hand side of the discontinuity is equal to the elevation of the crest of the sawtooth, therefore the top of the sawtooth is dry and part of the rarefaction wave is supercritical. Configurations 4a-b use the bottom elevation profile $z_{b,1}(x)$, while configurations 4c-d use the profile $z_{b,2}(x)$.

Test	$z_b(x)$ function	z_L	z_R
4a	$z_{b,1}(x)$	0.2 m	0.1 m
4b	$z_{b,1}(x)$	0.2 m	0.05 m
4c	$z_{b,2}(x)$	0.2 m	0.1 m
4d	$z_{b,2}(x)$	0.2 m	0.05 m

Table 7: Test 4: dambreak over microtopography. Configuration nomenclature.

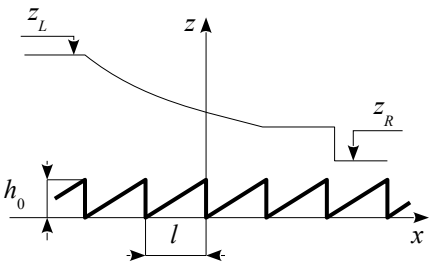

Figure 16: Test 4: dambreak over microtopography. Definition sketch for bottom profile $z_{b,1}(x)$.

The DDP model is used with the IP and DIP closures. The drag coefficient $C_{D,1}$ and the momentum dissipation coefficient μ_{xx} are calibrated so as to obtain an optimal fit of the front speed against the period-averaged output of the refined two-dimensional shallow water model (Table 8).

Test	Closure	$C_{D,2}$	μ_{xx}
4a, 4c	IP	0.	0.
4a, 4c	DIP	0.	0.
4b, 4d	IP	0.	0.2
4b, 4d	DIP	0.	0.5

Table 8: Test 4: dambreak over microtopography. Calibrated momentum dissipation parameters.

The resulting average water depth and unit discharge profiles computed at $T = 5\,\mathrm{s}$ are shown on Figure 17. The following remarks can be made on the respective performance of the IP and DIP closures.

For Tests 4a and 4c, the IP closure consistently yields an underestimated shock speed and overestimated post-shock unit discharge compared to the refined 2D model simulation. This is true for $C_{D,2} = \mu_{xx} = 0$. Increasing any of the two coefficients only contributes to slow down the shock in the DDP-IP solution, thus increasing the discrepancy with the refined 2D solution. For Tests 4b and 4d, the IP closure allows a correct shock speed to be recovered by setting $\mu_{xx} = 0.2$. While an accurate water depth shock profile is obtained (see second and fourth left-hand side graphs on Figure 17), the post-shock water depths are underestimated compared to the refined 2D shallow water solution. The post-shock unit discharge remains overestimated by approximately 25%.

The DIP closure allows more accurate average water depths and unit discharge profiles to be obtained. Calibrating $\mu_{xx} = 0$ for Tests 4a,c and $\mu_{xx} = 0.5$ for Tests 4b,d yields accurate shock speeds and unit discharge profiles. It is noted, however, that the water depth in the post-shock region is slightly underestimated compared to the reference, refined 2D solution.

It is also worth noting that the refined 2D shallow water model yields different water depth and unit discharge profiles depending on the bottom functions used ($z_{b,1}(x)$ or $z_{b,2}(x)$). This is clearly visible on Figure 17. The period-averaged water depth and unit discharge profiles (dotted profiles on the Figure) are different for Tests 4a and 4c. The same is observed for Tests 4b and 4d. The bottom profile function $z_{b,1}(x)$ yields sharper refined 2D profiles than does the bottom profile function $z_{b,2}(x)$. Moreover, the unit discharge profile exhibits a plateau in Test 4a, while it slightly decreases with (x/t) in Test 4c. However, from a macroscopic point of view, the two configurations $z_{b,1}(x)$ an $z_{b,2}(x)$ (41a, 41b) are described by exactly the same porosity functions (42a, 42b). This shows that (i) the porosity alone is not a sufficient descriptor of the subgrid-scale feature of the flow field, (ii) different momentum source terms model may be needed depending on the direction of the flow with respect to the topographical/geometric fluctuations on the subgrid scale.

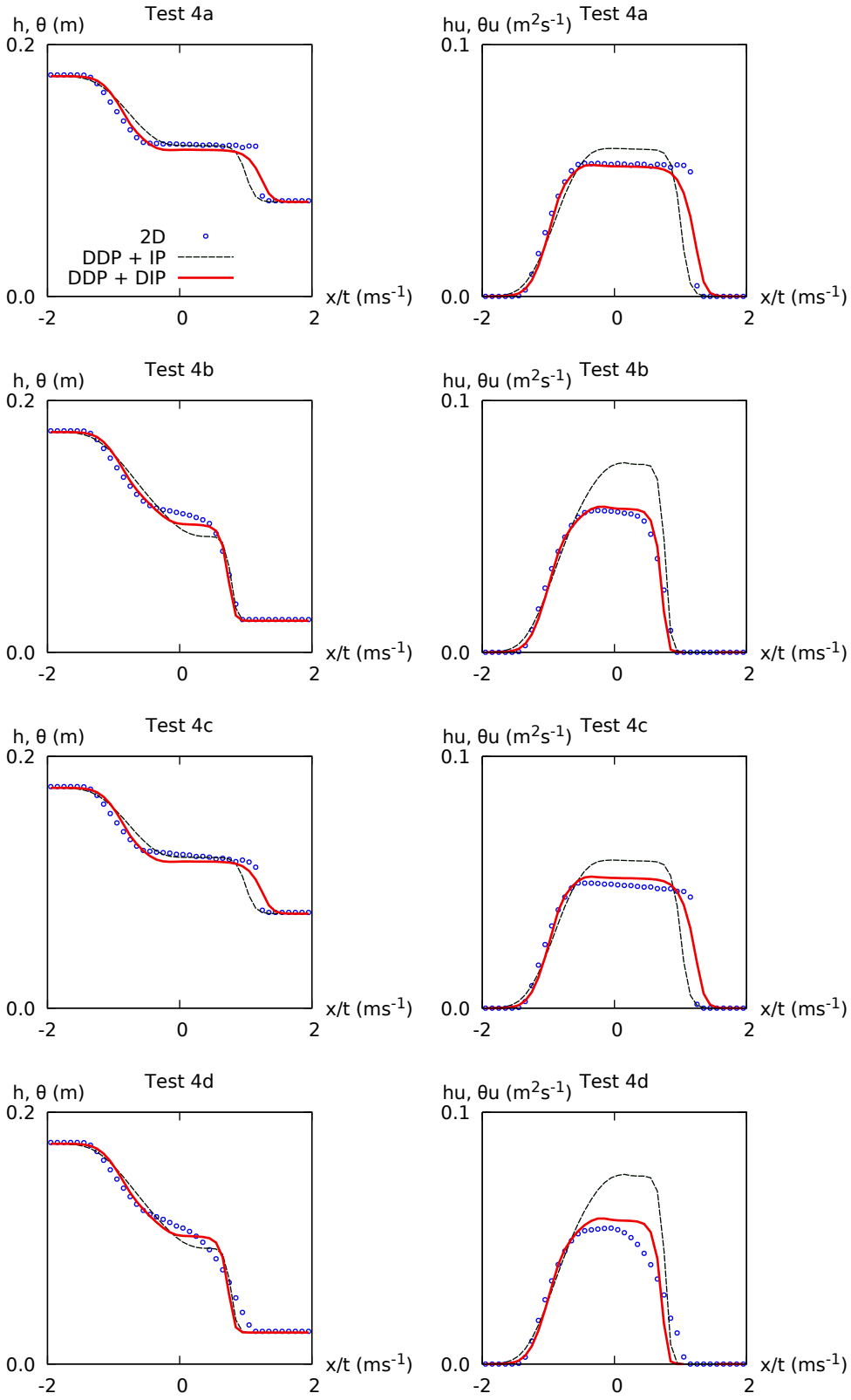

Figure 17: Test 4: dambreak over microtopography. Average water depth and unit discharge profiles at t =5s. Dots: refined 2D shallow water model solution, averaged over the wavelength l. dashed line: DDP-IP model. Solid line: DDP-DIP model.

Lastly, one may question the method of calibrating the model via the coefficient μ_{xx}, while the drag coefficient $C_{D,2}$ is set to zero in all four configurations. That the best fit would be achieved by tuning μ_{xx} was unexpected. In the light of Subsection 2.5, the effect of the roughness induced by the sawtooth bottom profile should be expected to be accounted for by the obstacle overflow drag coefficient $C_{D,2}$. However, calibrating the porosity model using this coefficient is seen to be inefficient: the drag term $\mathbf{f}_{D,2}$ fails to reconstruct the water depth and unit discharge profiles of the period-averaged refined 2D model. This is illustrated by Figure 18. On this figure, μ_{xx} is set to zero in the DDP-DIP model, while three different values (namely 0.1, 0.5 and 1.2) are used for $C_{D,2}$. While increasing $C_{D,2}$ yields a more accurate shock speed, it does not allow a correct shape to be recovered for the water depth profile. Moreover, the unit discharge is reduced dramatically compared to the solution computed by the refined 2D model.

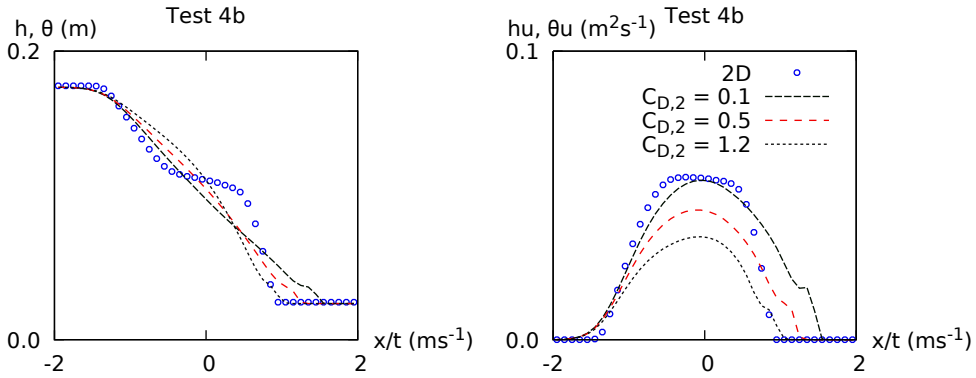

Figure 18: Test 4: dambreak over microtopography. Calibration of the obstacle overflow drag coefficient $C_{D,2}$.

4.5 Test 5: wave propagation in a meandering channel

The fifth test consists in simulating the propagation of a surge wave in a meandering channel with sharp bends. The purpose is to check the discretization of boundary conditions and the ability of the model to take into account the influence of abrupt direction changes in the flow geometry. Such channels are found in e.g. coastal lagoons. In such systems, the connection dynamics between two given lagoons, or between the lagoons and the sea, may be primarily driven by such channels [5, 16].

A similar test was presented in [49], with water flowing in a U-bend. However, in [49] only a single bend was modelled, with a smooth geometry. In the present test, the bends are intentionally made sharp, so as to induce more complex flow patterns than with a smooth geometry. A two metre wide channel with 45 degrees and 90 degrees bends is defined, with the geometry shown on Figure 19. The bottom is flat, motion is assumed frictionless. The water is initially at rest, with a uniform water level z_0. At $t = 0$, the water level at the upstream end of the channel (left-hand side of the sketch on Figure 19) is set instantaneously to z_{us}. The water level at the downstream end (right-hand side of the sketch) is kept to the constant value $z_{\text{ds}} = z_0$. The parameters of the test case are given in Table 9.

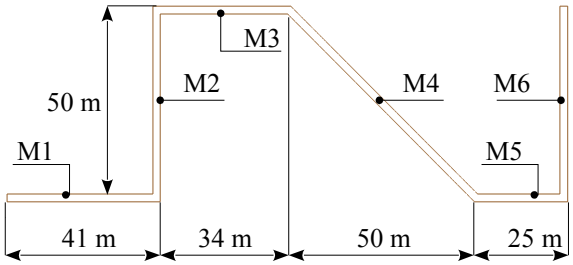

Figure 19: Test 5: wave propagation in a meandering channel. Plan view definition sketch.

Symbol	Parameter	Numerical value
W	Channel width	2 m
z_0	Initial water level	1 m
z_b	Bottom level	0 m
z_{ds}	Prescribed downstream water level	1.0 m
z_{us}	Prescribed upstream water level	1.1 m

Table 9: Test 5: wave propagation in a meandering channel. Test case parameters.

Two models are built using two different meshes. The first model uses a high-resolution mesh to solve the two-dimensional shallow water equations. The channel is meshed by 20 cells across (Figure 20, top). The second model uses the DDP approach, and the mesh cells are three times as wide as the actual channel (thus 6 metres instead of 2 metres, see Figure 20, bottom), with both the storage and connectivity porosities set to 1/3:

$$\phi_\Omega(z) = \phi_\Gamma(z) = \begin{cases} 0 & \text{if} \quad z < z_b \\ \frac{1}{3} & \text{if} \quad z \geq z_b \end{cases} \tag{43}$$

Multiplying the cell size by 3 compared to the actual size of the channel allows the number of cells used to mesh the model to be divided by 3 while keeping the cells as close to square cells as possible, a key issue to minimize numerical diffusion.

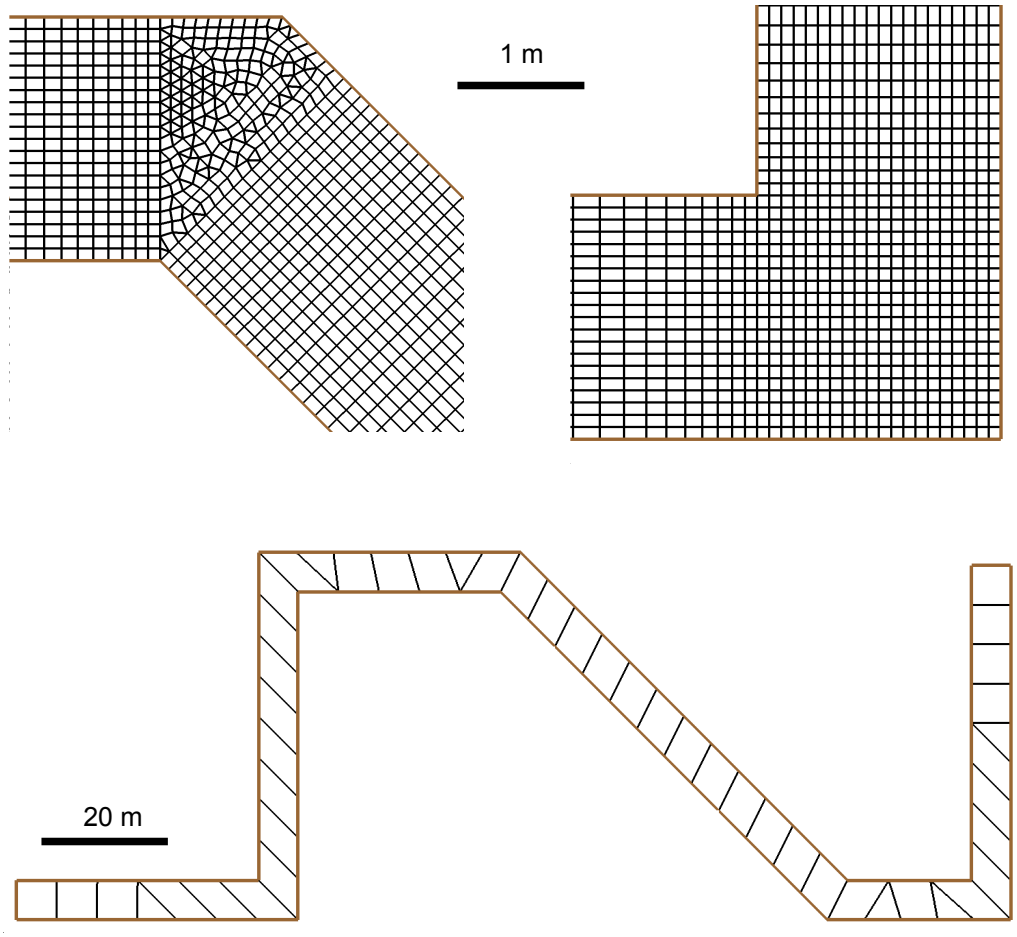

Figure 20: Test 5: wave propagation in a meandering channel. Top: zoomed view of the refined 2D mesh. Bottom: DDP model mesh.

Six points are defined in the middle of the six rectilinear reaches of the channel (see Figure 19). They are labelled from M1 to M6. Figures 21 and 22 show the free surface elevations and the unit discharges computed at these points from $t = 0$ to $t = 300\,\mathrm{s}$. The DDP model is very successful in reproducing the variations in the water levels computed by the refined 2D model (Figure 21). Quite expectedly, the coarse grid of the DDP model yields a smoother $z_s\,(t)$ signal than that of the refined 2D model. This is explained by the much coarser grid and the inevitable numerical diffusion, that has much stronger and more visible effects in the DDP solution than in the refined 2D solution. This slight damping excepted, the DDP model reproduces successfully the time lag between the multiple wave reflections caused by the bends of the channel. Transient damping by the DDP model is confirmed by the examination of the unit discharges computed at points M1-6 (Figure 22). Until $t = 100\,\mathrm{s}$, the DDP solution is in remarkable agreement with that of the refined 2D model. After this time, the unit discharge computed by the DDP model is consistently underestimated compared to that of the 2D model. The DDP model starts deviating from the refined 2D model at point M6 first, at approximately $t = 100\,\mathrm{s}$. This coincides with the time at which the return wave, triggered by the reflection of the impinging wave against the downstream boundary, passes at the point M6. The time for which the DDP solution starts departing from the refined 2D solution increases as the wave travels back from point M6 to M1. The time lag of 100s between the two points M6-M1 is in agreement with the 300m covered by the wave between the two points at a speed $c = (gh_0)^{1/2} \approx 3.1\,\mathrm{ms}^{-1}$. This confirms that the deviation of the DDP model from the refined 2D model is due to an underestimation of the transient generated by the reflection of the wave against the downstream boundary. This is not surprising in

that the backward wave originating from the downstream boundary is a rarefaction wave, that tends to spread over time. The spreading (thus the damping of the dynamics) is obviously overestimated by the DDP model due to the coarse mesh.

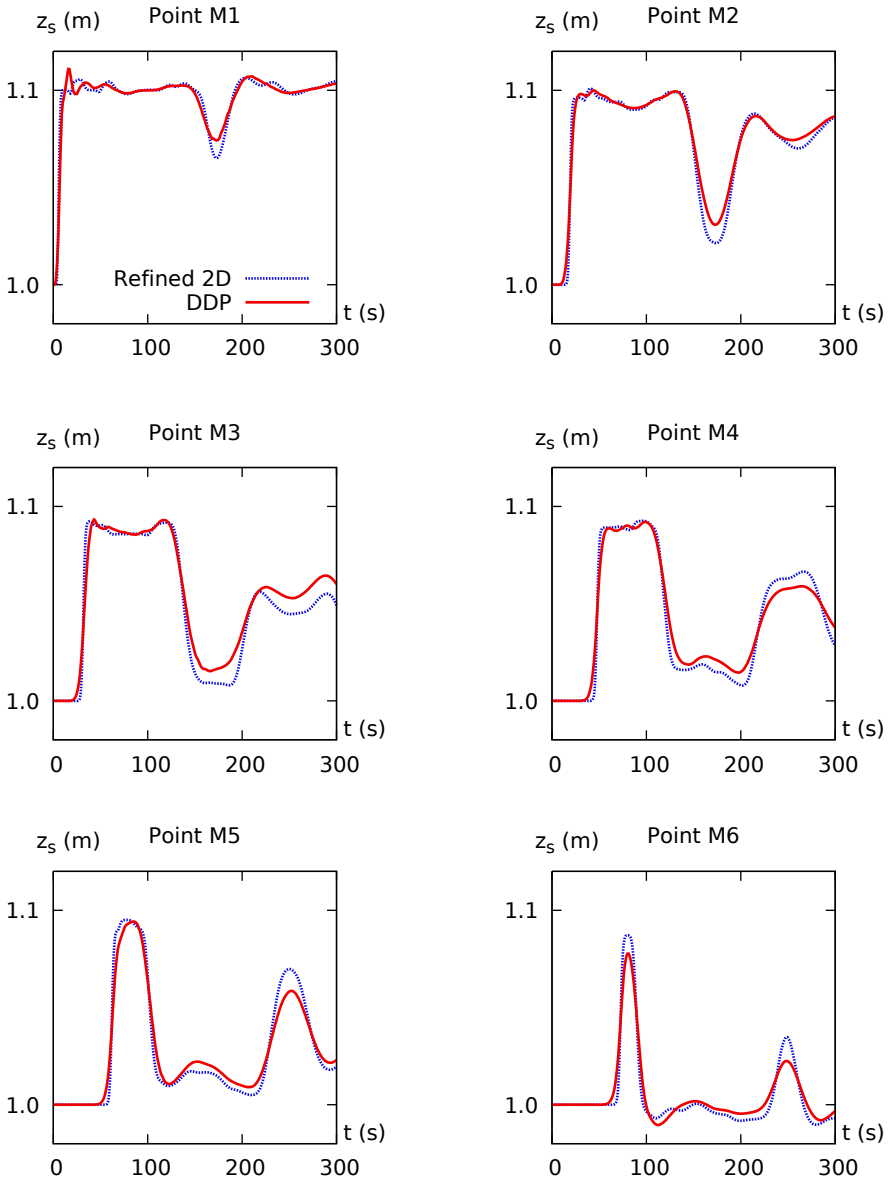

Figure 21: Test 5: wave propagation in a meandering channel. Free surface elevations computed by the refined 2D model and DDP model at Points M1-6.

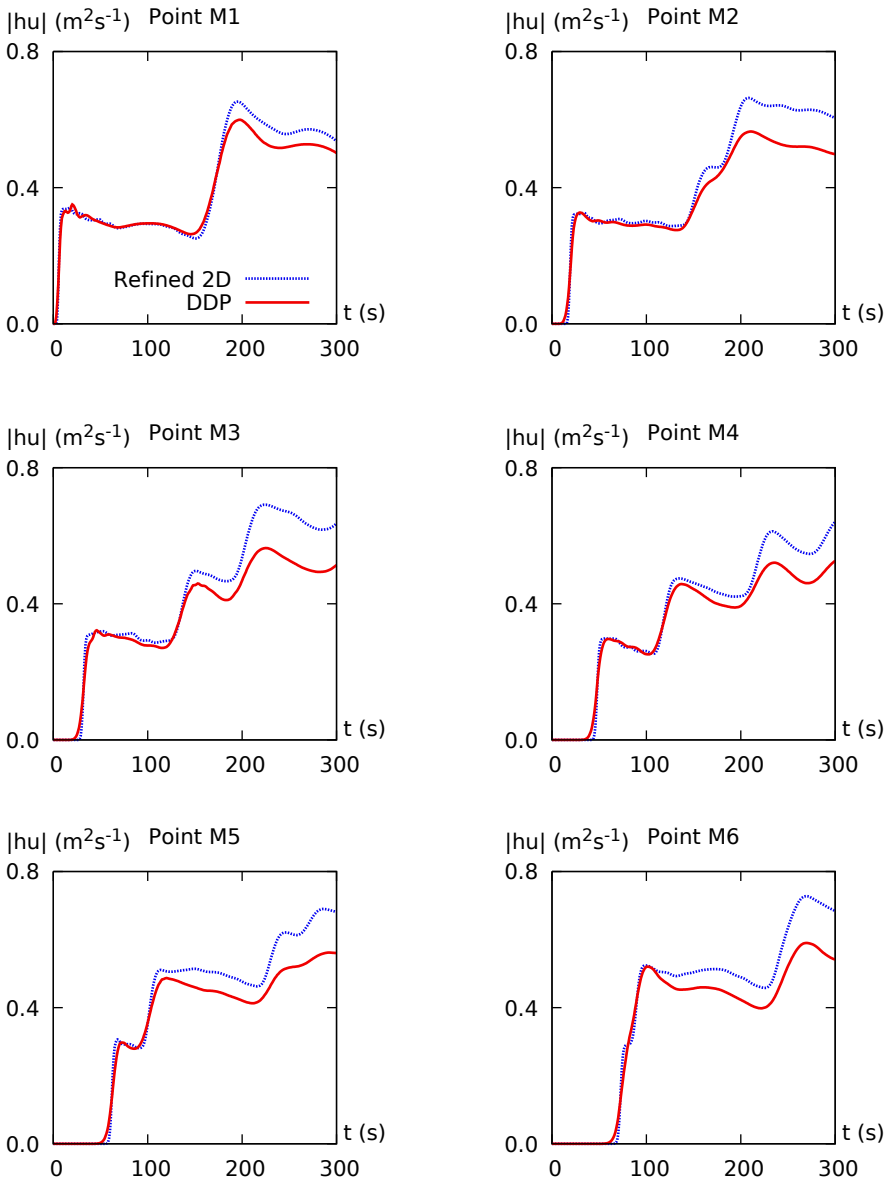

Figure 22: Test 5: wave propagation in a meandering channel. Unit discharges computed by the refined 2D model and the DDP model at Points M1-6.

4.6 Model CPU performance

The present subsection is devoted to an analysis of the CPU time gain provided by the DDP model over the refined 2D models used in Tests 1 to 5. All simulations were on an i7-core(TM) processor with 16GB RAM and 2.5GHz frequency. Table 10 shows the CPU times for the refined 2D and the DDP models for all the configurations. The DDP model is between 300 times and 3000 times as fast as the refined 2D model. In all applications, the CPU time required by the DDP model is two orders of magnitude smaller than the simulated time. In contrast, the refined 2D model sometimes requires more time than the simulated time.

Test	Simulated time	CPU time refined 2D model	DDP closure	CPU time DDP	2D/DDP CPU ratio
2a	50 s	53.4 s	IP / DIP	5.6×10^{-2}s	945
2b	50 s	35.86 s	IP / DIP	5.4×10^{-2} s	997
3a	100 s	69.66 s	IP	0.36 s	385
3a	100 s	69.66 s	DIP	0.31 s	450
3b	100 s	143.3 s	IP	0.39 s	734
3b	100 s	143.3 s	DIP	0.38 s	763
3c	100 s	46.1 s	IP	0.28 s	327
3c	100 s	46.1 s	DIP	0.26 s	360
3d	100 s	42.9 s	IP	0.27 s	317
3d	100 s	42.9 s	DIP	0.28 s	310
4a, 4c	10 s	49.4 s	IP	4.06×10^{-2} s	1215
4a, 4c	10 s	49.4 s	DIP	3.48×10^{-2} s	1415
4b, 4d	10 s	49.8 s	IP	3.59×10^{-2} s	1390
4b, 4d	10 s	49.8 s	DIP	4.21×10^{-2}	1180
5	300 s	857 s	IP / DIP	0.295 s	2900

Table 10: Performance of porosity vs. refined 2D model. Note: the plan view area of the 2D model for Tests 3a-d is half that of the DDP model. This is accounted for in the CPU time ratio.

5 Experimental validation

5.1 Experimental and model setup

In this section the depth-dependent porosity model is tested against an experimental data set involving topography submersion. The experiment consists in simulating the effect of a tsunami wave on an urban area next to the shoreline. The experiment is described in detail in [37], only an overview is given here for the sake of conciseness. A 1:50 undistorted scale model of the Seaside (Oregon) area was built at the O.H. HinsdaleWave Research Laboratory, Oregon State University. The scale model includes a portion of the sea bottom up to 1km from the shore line. A 500 m×600 m fraction of the urbanized area located along the shore is also included in the scale model. A schematic side view of the model is shown in Figure 23 (bottom). A high resolution lidar-surveyed topographical data set is available from the experiments. The topography within the 10 m×12 m urban area in the model is described by over 3×10^6 lidar points (Figure 23).

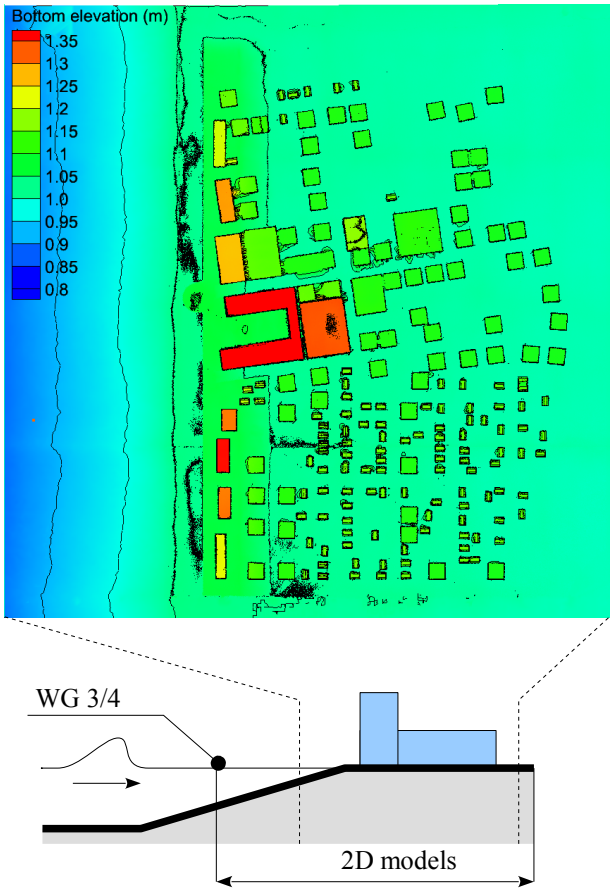

Figure 23: Seaside undistorted 1:50 scale model. Top: plan view of the lidar-based topography over the urban area. Bottom: definition sketch of the scale model.

The tsunami wave was simulated by a single move of a wave maker located approximately 30 m from the shoreline. The displacement of the wave maker vertical wall followed an error function of time. The water level was recorded as a function of time using 4 surface piercing resistive gauges in the basin. Within the urban area, 4 pairs of ultrasonic gauges were used to measure the water depth. These gauges were moved in unison over 9 transects. A total 31 measurement locations are available in the water level data set. Replicating the experiments led to ensemble-averaged water depth time series.

The experiment reported in [37] is simulated using two models. The first is the classical two-dimensional shallow water model with a detailed meshing of the geometry. The second is the proposed DDP-DIP model, with a much coarser mesh (the computational cells may be bigger than some of the buildings). The purpose is to assess (i) whether the depth-dependent porosity model is able to reproduce the experimental results satisfactorily, and (ii) the amount of information lost by the DDP model compared to the more detailed shallow water model. Table 11 gives the main characteristics of the two meshes. The DDP model has almost 30 times as few cells as the shallow water model. Figure 24 shows a zoomed view of the fine mesh within the urban area. The main streets are meshed using 5 to 10 cells across. Since the buildings may be submerged, they are included in the mesh.

Item	Refined 2D model	Porosity model
Total number of cells	92615	3305
Average cell area	$5.75 \times 10^{-3}\,\mathrm{m}^2$	$1.61 \times 10^{-1}\,\mathrm{m}^2$
Number of cells in urban area	63557	1457
Average cell area	$2.39 \times 10^{-3}\,\mathrm{m}^2$	$1.04 \times 10^{-1}\,\mathrm{m}^2$

Table 11: Seaside scale experiment. Model characteristics. The urban area is defined as the rectangular area $(x, y) \in [33.08, 43.50] \times [-6.053, 8.45]$ (coordinates in metres as in Park et al. (2013)).

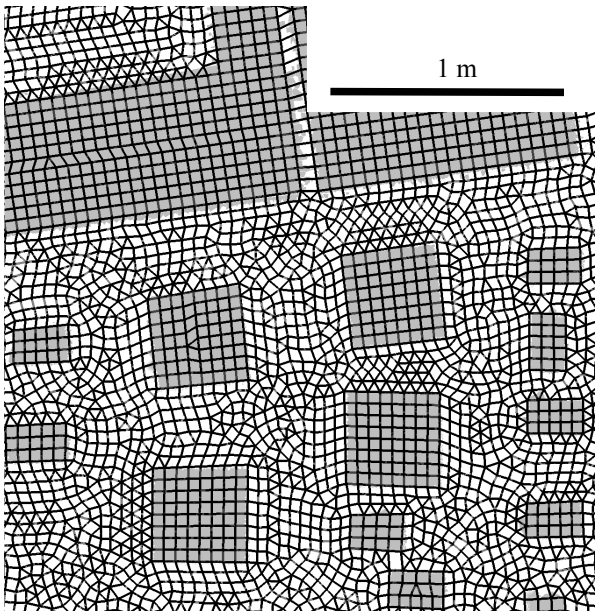

Figure 24: Seaside scale experiment. Refined 2D shallow water model. Detailed view of the mesh.

Figure 25 shows the computational grid of the DDP model over the entire urban area. The depth-dependent porosity laws are defined piecewise uniform over 16 polygons. These polygons (bold lines in the Figure) are defined as areas of uniform building geometry and density.

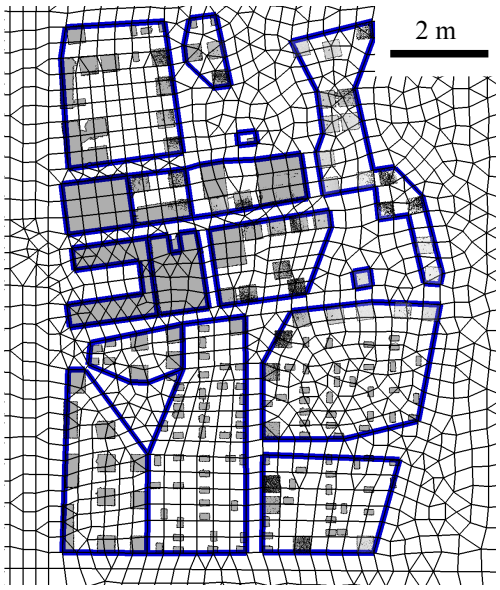

Figure 25: Seaside scale experiment. DDP model. Mesh of the urban area and polygons delinating the zones of uniform porosity law pairs.

A single $(\phi_\Omega(z), \phi_\Gamma(z))$ law pair is defined for each of the 16 polygons. This $(\phi_\Omega(z), \phi_\Gamma(z))$ pair is applied to all the cells and interfaces that belong to the polygon. Since the building roofs are almost flat, the $\phi(z)$ laws are defined as piecewise constant. ϕ is constant from the ground level to the roof level. Above the roof level, it is equal to unity. The values of ϕ_Ω and ϕ_Γ are obtained by measuring the areas and base lengths of the buildings on the edges of the polygons. Subtracting these areas and lengths from those of the polygons yield the storage and connectivity area. Normalizing by the polygon area and perimeter yields the $\phi_\Omega(z)$ and $\phi_\Gamma(z)$ laws. Note that using a uniform $(\phi_\Omega(z), \phi_\Gamma(z))$ law pair over predefined polygons is not the only possible way of deriving the porosity laws. For depth-independent integral porosity models, the building footprint approach is more often used (see e.g. [39, 24]). In the present study, the uniform law pair approach was preferred for the following reasons. Firstly, the building footprint approach is known to induce significant mesh dependency when the connectivity porosity field is not uniform [22]. The piecewise uniform porosity approach minimizes this issue. Secondly, the purpose was also to assess the influence of the resolution of the porosity field on model accuracy. Two meshing approaches were used for this. The first consists in including the main streets within the porosity polygons. This is the case with gauges A1-6 (Figure 26). The second approach consists in excluding the main streets from the porosity polygons, as done with the streets B1-6 and C1-6 in Figure 26. In the streets, depth-independent, unity porosity values are used. The first approach induces milder meshing constraints than the second one, but is expected to be less accurate in predicting point values of the flow field. Indeed, the porosity approach is known to be efficient in simulating averaged flow fields over spatial extents at least as large (if not larger) than the building period [23].

5.2 Model results and performance

In the experiment reported in [37], the movement of the wave maker started at $t = 15\,\mathrm{s}$. Therefore, the time interval [0 s, 15 s] was not simulated and the simulation period is [15 s, 40 s]. Bearing in mind the 1:50 scale and assuming Froude similarity, the simulated 25 s would correspond to $25 \times 50^{1/2} = 177\,\mathrm{s}$ for the full scale transient. Table 12 gives the CPU times for the refined 2D and DDP models. The CPU time ratio between the two is over 70. The Manning friction coefficient was calibrated in the refined 2D model so as to obtain the best possible fit with the experimental water depth time series. The optimal value was found to be $n_M = 10^{-3}\,\mathrm{m}^{1/3}\mathrm{s}^{-1}$, which is approximately 20 times as small than typical Manning coefficient values in urban areas. It should be kept in mind however that (i) the magnitude of flow velocities, water depths and transient durations involved in the present experiment are much smaller than those of typical full scale events, (ii) the friction factor reported in [37] is commensurate

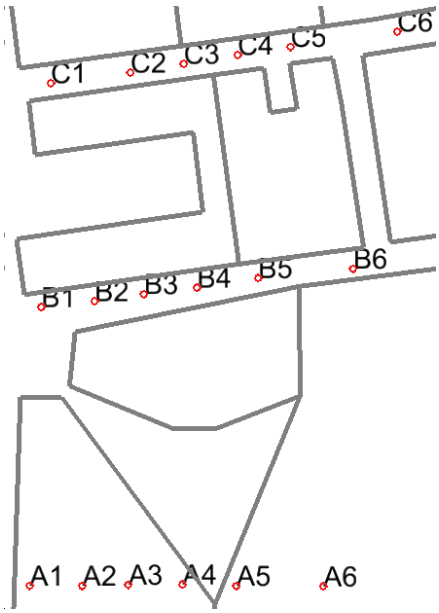

Figure 26: Seaside scale experiment. Locations of the experimental gauges and meshing approaches.

with such Manning values. The friction formula used in [37] involves a quadratic function of the flow velocity for the shear stress [28]. Identifying this model with the Manning bottom friction model yields:

$$\frac{f}{4\rho}\left\|\mathbf{u}\right\|\mathbf{u} = gh^{-1/3}n_M^2\left\|\mathbf{u}\right\|\mathbf{u} \Longrightarrow n_M = \left(\frac{fh^{1/3}}{4\rho g}\right)^{1/2} \tag{44}$$

where f is the friction factor and ρ is the water density. In [37], the optimal values for f are reported to be in the range from 10^{-3} to 10^{-2}. With typical h values of 0.1 m, this corresponds to n_M values ranging from 10^{-4} to $3\times10^{-4}\,\mathrm{m}^{1/3}\mathrm{s}^{-1}$. This is even smaller than the optimal n_M value found for the refined 2D model. However, the model used in [37] incorporates dispersive stresses that are not accounted for in the shallow water model. This may explain the difference between the two models. The calibrated $n_M = 10^{-3}\,\mathrm{m}^{1/3}\mathrm{s}^{-1}$ was used directly in the DDP model. Another point worth noting is that the porosity model results were found insensitive to the momentum dissipation coefficient. This is attributed to the small velocities generated by the transient.

Table 12 about here

Model	CPU time
Refined 2D	1490 s
DDP-DIP	20.5 s

Table 12: Seaside experiment. CPU times for the refined 2D and DDP models. Simulated time: 25 s.

Figure 27 shows the simulation results at six locations. Gauges A1 and A6 are located along a main street that is not meshed explicitly in the DDP model. In contrast, gauges B1, B6, C1 and C6 are located in two streets accounted for explicitly in the porosity model mesh. Gauges A1, B1 and C1 are located within the front row of buildings, while gauges A6, B6 and C6 are located well into the urban area. The Following conclusions can be drawn from the figure.

Firstly, both the refined 2D and the porosity model overestimate the propagation speed of the incoming wave. The simulated wave arrives at gauges A1-C1 1 s to 1.5 s earlier than the recorded wave. This could be attributed to the shallow water model, that fails to incorporate the dispersive stresses induced by non-hydrostatic effects. However, a similar shift is observed in the water depth simulated by the non-hydrostatic COULWAVE model (see e.g. Figure 7 in [37]). Another explanation for this is that the $z_s\left(t\right)$ boundary condition supplied at the Western boundary of the model is not accurate enough owing to non-hydrostatic effects.

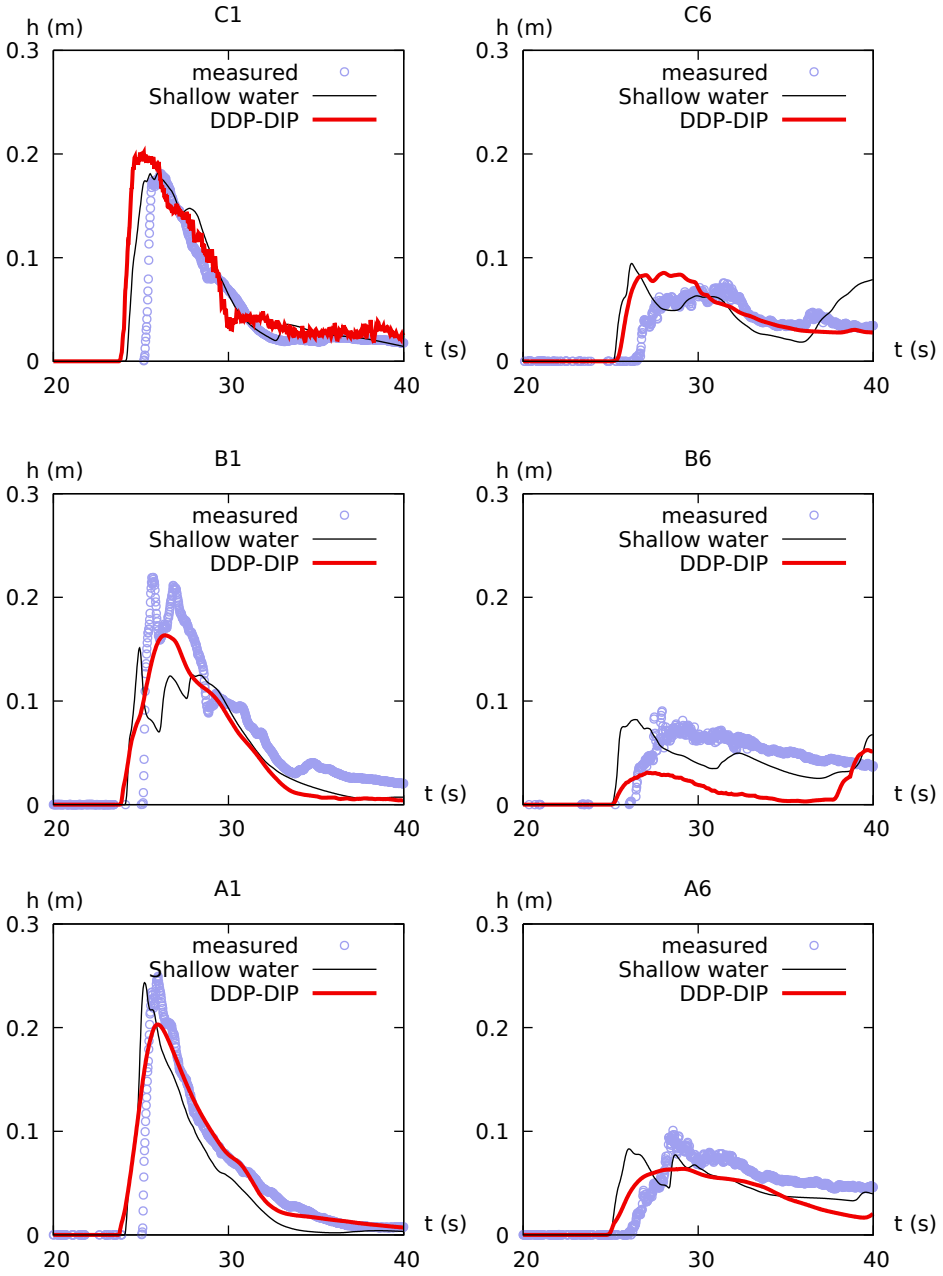

Figure 27: Seaside experiment. Water depths as functions of time at six depth gauges. Dots: experimental values. Thin line: refined 2D model. Bold line: depths-dependent porosity model. The rising water levels at the end of the simulation period are due to backwater effects from the model boundary.

Secondly, the accuracy of the porosity model is similar to that of the refined 2D model. The only exception is Gauge B6, where the water depth is strongly underestimated by the DDP model. The reason for this was found to be an overestimated flow into the lateral streets in the neighbourhood of gauge B6. This shows the limitations of assigning uniform porosity laws over large areas.

Thirdly, the water levels simulated by the porosity model at gauges A1 and A6 are surprisingly accurate considering that the street A1-6 is not meshed explicitly. This is all the more surprising as comparing the results of the porosity model (that results from an averaging) to point values is known to induce errors [29]. This is interpreted as a confirmation that major urban axes may be included in porosity models without degrading significantly the accuracy of the simulations.

6 Discussion

The tests presented in Sections 4-5 illustrate the potential of the DDP model to account for the large scale features of shallow water flows in the presence of complex geometries. As far as flood hazard mapping is concerned, however, the pore scale averaged values of the flow variables provide an incomplete insight into the actual distribution of the flood risk. Maximum risk is usually encountered at points of large water depths and/or large flow velocities. Flood hazard mapping thus requires an assessment not only of the average flow fields, but also of extreme flow field values on the local scale [4]. The question arises whether the average values provided by the DDP model are sufficient for this. This question is partly answered by examining the results of Tests 2 and 3. A similar analysis could be carried out for the other tests presented in this paper. For the sake of conciseness, the discussion is restricted to these two tests. The free surface elevation, flow velocity and depth-velocity product profiles computed by the DDP model are compared to those computed by the 2D model on Figures 28 and 29 for Test 2a and Test 2b respectively.

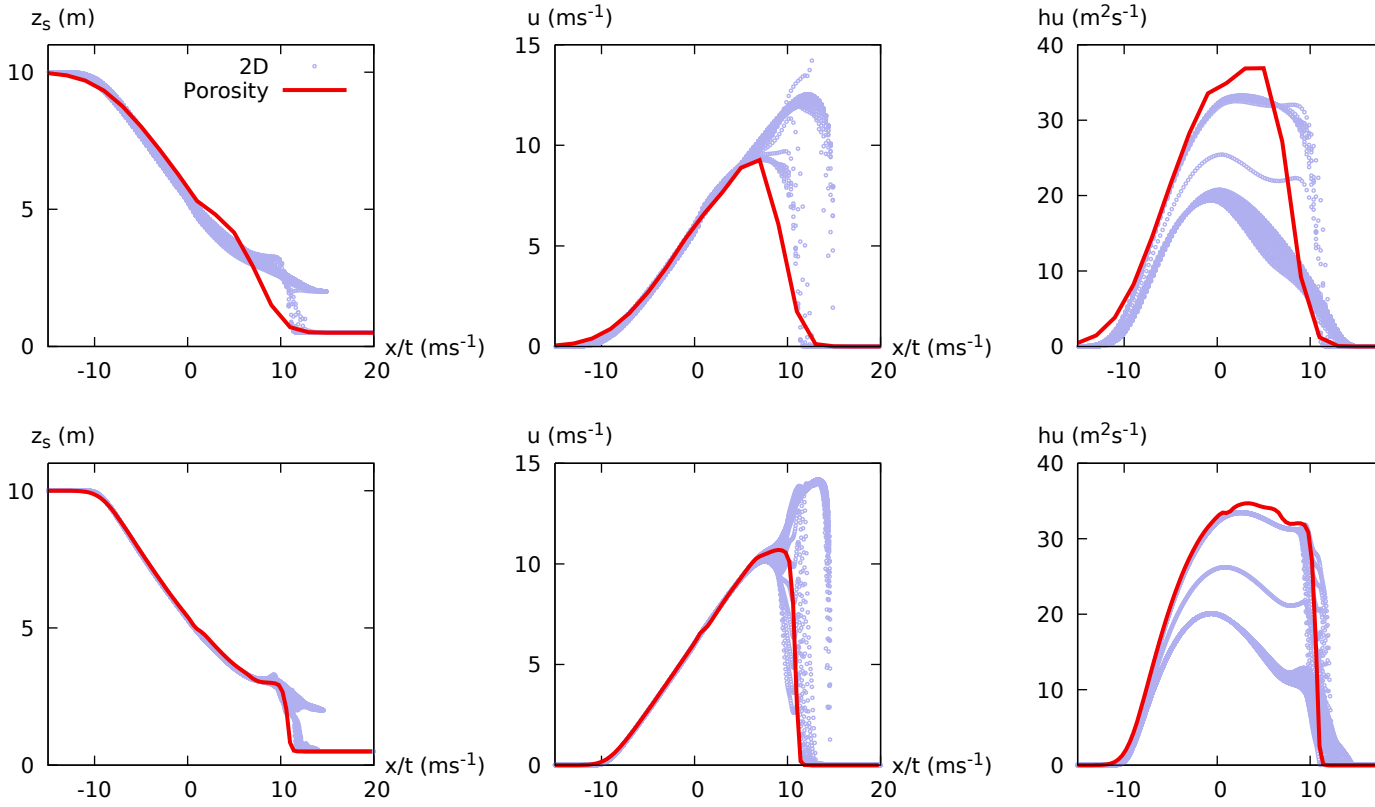

Figure 28: Dambreak in a compound channel. Simulation results for test 2a ($h_R = 0.5$m) at $t = 10$s (top) and $t = 50$s (bottom). Dots: free surface elevations, flow velocities and unit discharges computed by the refined 2D model. Solid lines: DDP model results.

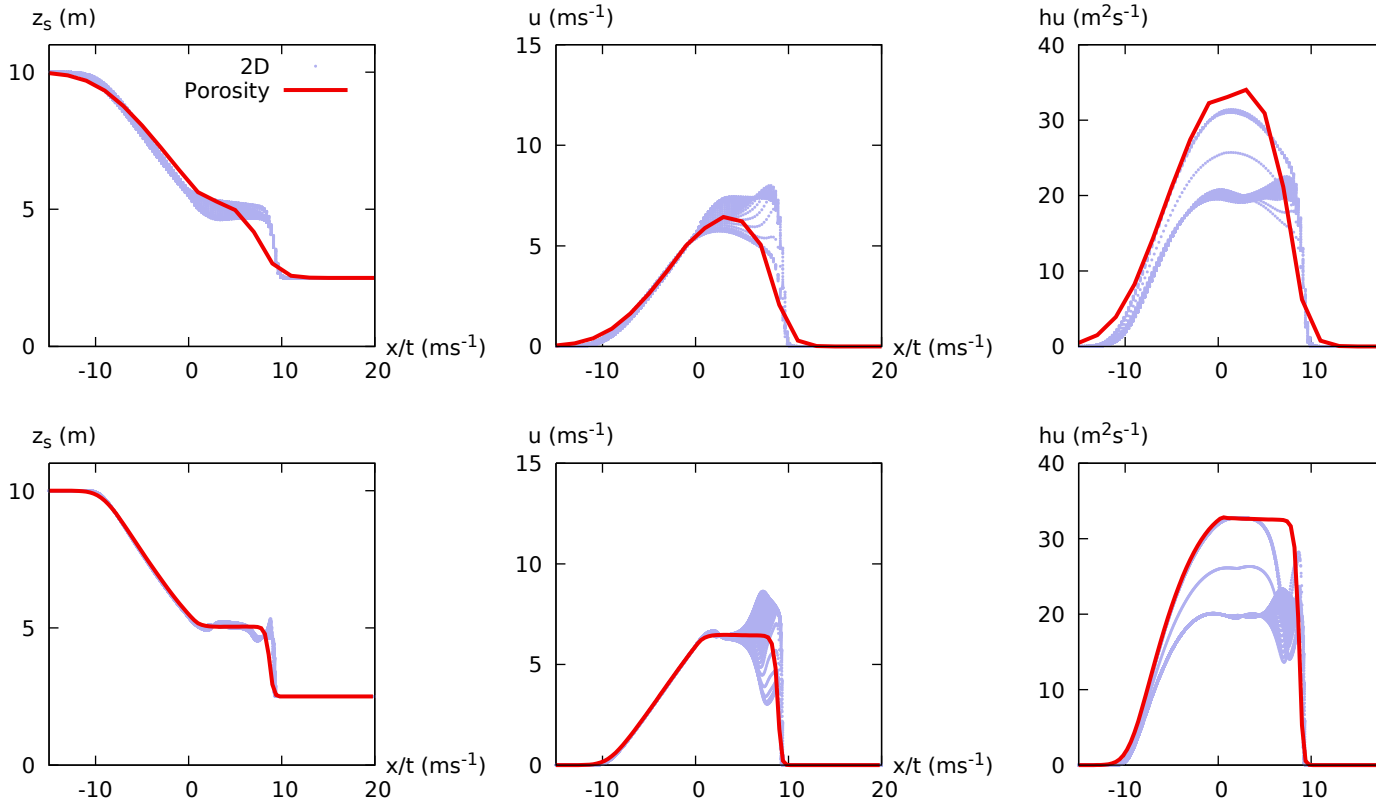

Figure 29: Dambreak in a compound channel. Simulation results for test 2b ($h_R = 2.5$m) at $t = 10$s (top) and $t = 50$s (bottom). Dots: free surface elevations, flow velocities and unit discharges computed by the refined 2D model. Solid lines: DDP model results.

Quite expectedly, the dispersion of the flow variables from the average values is larger in Test 2a than in Test 2b. As far as the free surface elevations are concerned (Figure 28, left), the refined 2D results clearly show the dual structure of the shock wave, with one front travelling over the floodplain (hence the floor value $z = h_0 = 2$m in the profiles) and the other travelling within the main channel. The DDP model, that uses a single free surface elevation variable, can obviously not capture such a feature. As a consequence, the large flow velocities in the advancing front over the floodplain are missed by the DDP model (Figure 28, middle). The maximum, point values of the flow velocity are underestimated by approximately 30% in the DDP flow velocity profiles. Lastly, the unit discharge hu profile in the refined 2D model is compared to the product hu obtained from the DDP model on Figure 28, right. Note that the unit discharge in the DDP model is not hu but θu (plotted on Figure 11, right). hu in the DDP model is fairly representative of the hu values in the refined 2D model, while θu coincides with the average 2D model values for hu. Similar, albeit smaller, deviations of the point values from the DDP averages are also observed in the simulation results for Test 2b (Figure 29). This was also to be expected in that Test 2b represents a less extreme hydraulic configuration than Test 2a, with smaller floodplain-channel exchanges.

As in test 2, the DDP-IP and DDP-DIP simulation results are compared to the cell values of the refined 2D shallow water model. The results for Test 3 are shown on Figure 30. The water levels in the refined 2D model are grouped into two sets, forming roughly parallel clouds. The lower of the two sets (ranging from 0 m to 5 m in Tests 3a-b and equal to 0 m in Tests 3c-d) corresponds to the water depths over the buildings, while the higher of the two clouds (ranging from 0 m to 10 m in Tests 3a-b and 0 m to 5 m in Tests 3c-d) corresponds to the water depths over the streets. The variability in the unit discharges is much stronger than in Test 2.

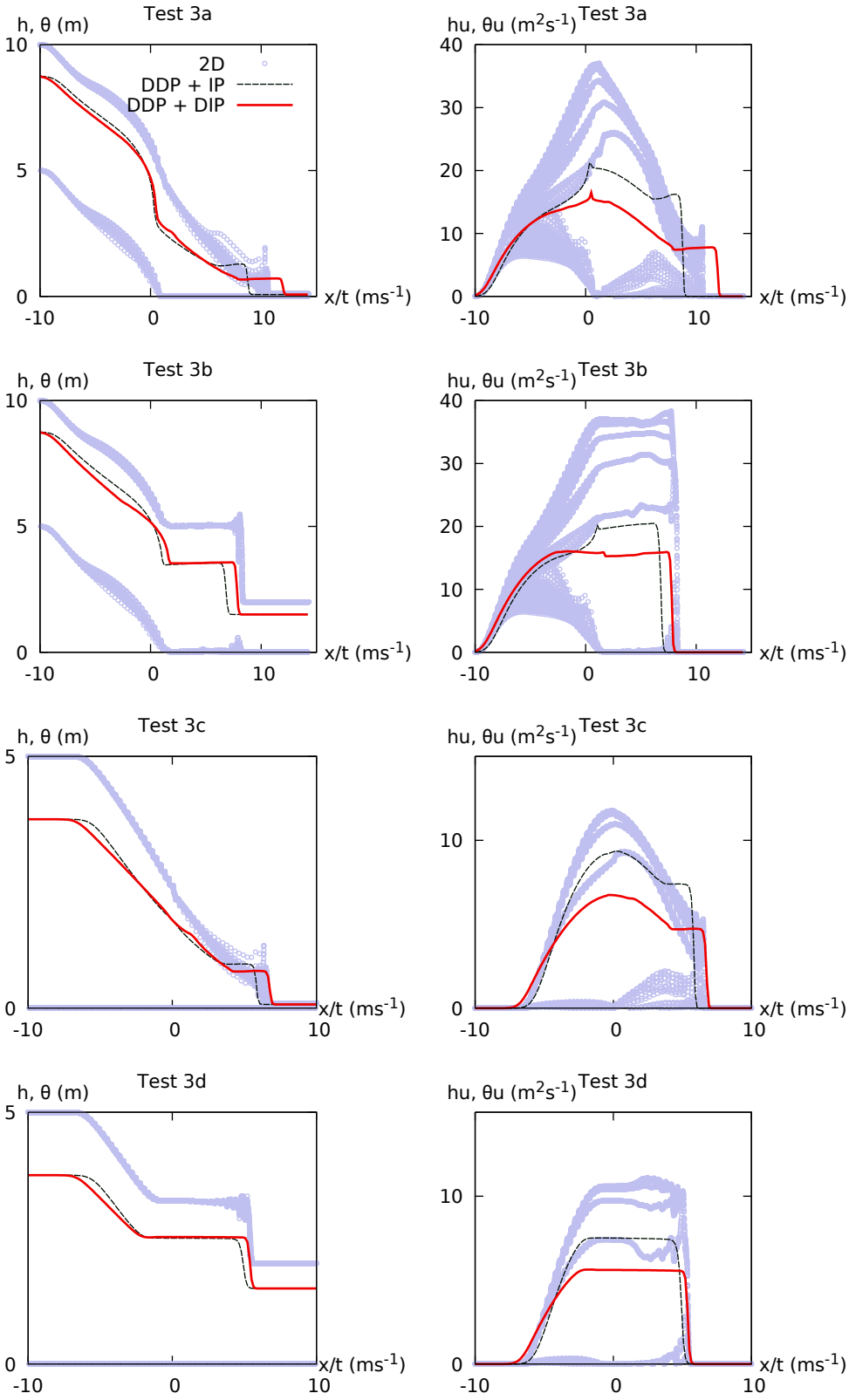

Figure 30: Urban dambreak problem (Test 3). Simulation results at $t = 70$s. Dots: water depths and unit discharges computed by the 2D shallow water model. Solid lines: DDP model solutions. Note that h is the water depth for the 2D shallow water model.

7 Conclusions

A depth-dependent porosity model has been presented. Compared to similar models previously presented in the literature [13, 48, 35, 34], the proposed model has the following features.

(i) The flux closure model between the domain- and the boundary-based flow variables uses the DIP closure proposed in [24], while the previously published DDP models use either the Single Porosity (SP) closure [13, 48] or the Integral Porosity (IP) closure [35, 34]. When used in depth-independent porosity models, the DIP closure is known to be more accurate than the SP and IP laws [23, 24]. The computational examples presented in the present paper allow this conclusion to be extended to depth-dependent porosity models. Compared to the depth-independent closure, the depth-dependent DIP closure requires an energy-based limiting of the flow velocity as the connectivity porosity tends to zero.

(ii) Obstacle-induced drag forces are broken into two terms. The first is due to the drag forces induced by the lateral walls of the obstacles, and acts only on the part of the flow that is lower than the height h_0 of the obstacles. The second is due to the friction and energy losses induced by the top of the obstacles when these are submerged. Consequently, it is not active at all times. Test 3 shows that this term is essential to an accurate reconstruction of the pore scale-averaged flow fields in the presence of submerged obstacles.

(iii) The DDP model also incorporates the transient momentum dissipation term $\mathbf{f}_T$ first introduced in the depth-independent DIP model [24]. This term is seen to be essential to a correct reconstruction of the flow fields computed by refined 2D models. This transient momentum dissipation mechanism was initially proposed to account for the energy dissipation triggered by positive waves flowing between series of obstacles. However, Test 4 shows that this mechanism is also more efficient than drag coefficient-based models in reproducing the energy losses caused by the sawtooth-shaped microtopography. This can be attributed to the momentum dissipation induced by the mobile bores generated as the wave propagates onto the microscale topography.

The tests presented in Section 4 show that all these features are essential to the DDP-IP model performance. Dropping one of them entails a strong degradation in model performance for one or several of the tests presented in Section 4. The Seaside test case presented in Section 5 shows that the accuracy of the DDP model in reproducing the general features of the flow is similar to that of the refined 2D shallow water model, with a much cheaper computational cost.

Future research includes several paths. The first is obviously the parametrization of the models for the terms $\mathbf{f}_{D,1}$, $\mathbf{f}_{D,2}$ and $\mathbf{f}_T$. While the models presented in Subsection 2.5 allow for a successful modelling of the large scale flow fields (see Section 4), how they should be parameterized as functions of the subgrid-scale geometric properties is still unclear. As a result, the drag and momentum dissipation tensors must be calibrated. Simulation bases such as that presented in [23] should be extended so as to allow for the parametrization of these energy dissipation models, thus eliminating the need for calibration. The second research path concerns the modelling of bottom friction. The Chezy-Manning-Strickler approach remains widely popular. However, experimental studies involving complex topographies and small depths indicate that alternative models, such as Reynolds-dependent friction models [18], might be more appropriate. For applications in natural environments, drag models incorporating vegetation mechanical properties [30, 50] will be needed too. Test 4 also shows that, for a given flow direction, the drag term may change as the flow is reverted. As illustrated by Section 5, a third research path should be devoted to the development of subgrid-scale models, that will allow the subgrid-scale features of the flow to be inferred from the large scale flow fields computed by the DDP models.

Acknowledgements

The authors wish to thank Dr H. Park and Prof. D. T. Cox at Oregon State University for kindly providing the experimental data from [37] used in Section 5.

Appendix A. Wave propagation speeds

A.1 IP model

For the IP model, the first column of the flux tensor is

$$\mathbf{f}_x = \left[\frac{\theta_\Gamma}{\theta_\Omega} q_\Omega, \frac{\theta_\Gamma q_\Omega^2}{\theta_\Omega^2} + f_{w,\Gamma}, \frac{\theta_\Gamma q_\Omega r_\Omega}{\theta_\Omega^2}\right]^T \tag{45}$$

It is first noticed that the water level closure (17a) induces a one-to-one relationship between θ_Γ and θ_Ω. Consequently, the derivative of θ_Γ with respect to θ_Ω is derived as

$$\frac{\mathrm{d}\theta_\Gamma}{\mathrm{d}\theta_\Omega} = \frac{\mathrm{d}\theta_\Gamma}{\mathrm{d}z}\frac{\mathrm{d}z}{\mathrm{d}\theta_\Omega} = \frac{\phi_\Gamma}{\phi_\Omega} \tag{46}$$

For the Jacobian matrix, the following quantities must be determined

$$\frac{\partial}{\partial\theta_\Omega}\left(\frac{\theta_\Gamma}{\theta_\Omega} q_\Omega\right) = \left(\frac{\phi_\Gamma}{\phi_\Omega} - \frac{\theta_\Gamma}{\theta_\Omega}\right) u_\Omega \tag{47a}$$

$$\frac{\partial}{\partial q_\Omega}\left(\frac{\theta_\Gamma}{\theta_\Omega} q_\Omega\right) = \frac{\theta_\Gamma}{\theta_\Omega} \tag{47b}$$

$$\frac{\partial}{\partial r}\left(\frac{\theta_\Gamma}{\theta_\Omega} q_\Omega\right) = 0 \tag{47c}$$

$$\frac{\partial}{\partial\theta_\Omega}\left(\frac{\theta_\Gamma q_\Omega^2}{\theta_\Omega^2}\right) = \left(\frac{\phi_\Gamma}{\phi_\Omega} - 2\frac{\theta_\Gamma}{\theta_\Omega}\right) u_\Omega^2$$

$$\frac{\partial}{\partial q_\Omega}\left(\frac{\theta_\Gamma q_\Omega^2}{\theta_\Omega^2}\right) = 2\frac{\theta_\Gamma}{\theta_\Omega} u_\Omega \tag{47d}$$

$$\frac{\partial}{\partial r_\Omega}\left(\frac{\theta_\Gamma q_\Omega^2}{\theta_\Omega^2}\right) = 0 \tag{47e}$$

$$\frac{\partial f_{w,\Gamma}}{\partial\theta_\Omega} = \frac{\partial f_{w,\Gamma}}{\partial\theta_\Gamma}\frac{\partial\theta_\Gamma}{\partial\theta_\Omega} = \frac{\phi_\Gamma}{\phi_\Omega} c_\Gamma^2 = \frac{\theta_\Gamma}{\theta_\Omega} c_\Omega^2 \tag{47f}$$

$$\frac{\partial}{\partial\theta_\Omega}\frac{\theta_\Gamma q_\Omega r_\Omega}{\theta_\Omega^2} = \left(\frac{\phi_\Gamma}{\phi_\Omega} - 2\frac{\theta_\Gamma}{\theta_\Omega}\right) u_\Omega v_\Omega \tag{47g}$$

$$\frac{\partial}{\partial q_\Omega}\frac{\theta_\Gamma q_\Omega r_\Omega}{\theta_\Omega^2} = \frac{\theta_\Gamma}{\theta_\Omega} v_\Omega \tag{47h}$$

$$\frac{\partial}{\partial r_\Omega}\frac{\theta_\Gamma^2 q_\Omega r_\Omega}{\theta_\Omega^3} = \frac{\theta_\Gamma}{\theta_\Omega} u_\Omega \tag{47i}$$

hence the matrix $\mathbf{A}_x$

$$\mathbf{A}_x = \begin{bmatrix} \left(\frac{\phi_\Gamma}{\phi_\Omega} - \frac{\theta_\Gamma}{\theta_\Omega}\right) u_\Omega & \frac{\theta_\Gamma}{\theta_\Omega} & 0 \\ \left(\frac{\phi_\Gamma}{\phi_\Omega} - 2\frac{\theta_\Gamma}{\theta_\Omega}\right) u_\Omega^2 + \frac{\theta_\Gamma}{\theta_\Omega} c_\Omega^2 & 2\frac{\theta_\Gamma}{\theta_\Omega} u_\Omega & 0 \\ \left(\frac{\phi_\Gamma}{\phi_\Omega} - 2\frac{\theta_\Gamma}{\theta_\Omega}\right) u_\Omega v_\Omega & \frac{\theta_\Gamma}{\theta_\Omega} v_\Omega & \frac{\theta_\Gamma}{\theta_\Omega} u_\Omega \end{bmatrix} \tag{48}$$

The eigenvalue $\frac{\theta_\Gamma}{\theta_\Omega} u_\Omega$ stems directly from the last column of the matrix. The remaining two eigenvalues are those of the following 2×2 matrix

$$\mathbf{B}_x = \begin{bmatrix} \left(\frac{\phi_\Gamma}{\phi_\Omega} - \frac{\theta_\Gamma}{\theta_\Omega}\right) u_\Omega & \frac{\theta_\Gamma}{\theta_\Omega} \\ \left(\frac{\phi_\Gamma}{\phi_\Omega} - 2\frac{\theta_\Gamma}{\theta_\Omega}\right) u_\Omega^2 + \frac{\theta_\Gamma}{\theta_\Omega} c_\Omega^2 & 2\frac{\theta_\Gamma}{\theta_\Omega} u_\Omega \end{bmatrix} = \begin{bmatrix} \left(\frac{\phi_\Gamma}{\phi_\Omega} - \frac{\theta_\Gamma}{\theta_\Omega}\right) u_\Omega & \frac{\theta_\Gamma}{\theta_\Omega} \\ \left(\frac{\phi_\Gamma}{\phi_\Omega} - 2\frac{\theta_\Gamma}{\theta_\Omega}\right) u_\Omega^2 + \frac{\theta_\Gamma}{\theta_\Omega} c_\Omega^2 & 2\frac{\theta_\Gamma}{\theta_\Omega} u_\Omega \end{bmatrix} \tag{49}$$

The solution is

$$\lambda = \frac{1}{2}\mathrm{tr}\mathbf{B}_x \pm \left(\left(\frac{1}{2}\mathrm{tr}\mathbf{B}_x \right)^2 - \det \mathbf{B}_x \right)^{\frac{1}{2}} \tag{50a}$$

$$\det \mathbf{B}_x = \frac{\phi_\Gamma}{\phi_\Omega}\frac{\theta_\Gamma}{\theta_\Omega}u_\Omega^2 - \left(\frac{\theta_\Gamma}{\theta_\Omega}\right)^2 c_\Omega^2$$

=

$$\mathrm{tr}\mathbf{B}_x = \left(\frac{\phi_\Gamma}{\phi_\Omega} + \frac{\theta_\Gamma}{\theta_\Omega} \right) u_\Omega \tag{50b}$$

hence

$$\lambda = \frac{1}{2}\left(\frac{\phi_\Gamma}{\phi_\Omega} + \frac{\theta_\Gamma}{\theta_\Omega} \right) u_\Omega \pm \left(\frac{1}{4}\left(\frac{\phi_\Gamma}{\phi_\Omega} - \frac{\theta_\Gamma}{\theta_\Omega} \right) u_\Omega^2 + \left(\frac{\theta_\Gamma}{\theta_\Omega} \right)^2 c_\Omega^2 \right)^{\frac{1}{2}} \tag{51}$$

hence the three eigenvalues given in Equation (28a-28b).

A.2 DIP model

The first column of the flux tensor is

$$\mathbf{f}_x = \left[q_\Omega, \frac{q_\Omega^2}{\theta_\Gamma} + f_{w,\Gamma}, \frac{q_\Omega r_\Omega}{\theta_\Gamma} \right]^T \tag{52}$$

Following the same developments as in Subsection A.1, one obtains

$$\mathbf{A}_x = \begin{bmatrix} 0 & 1 & 0 \\ \frac{\theta_\Gamma}{\theta_\Omega}c_\Omega^2 - \frac{\phi_\Gamma}{\phi_\Omega}\frac{\theta_\Omega^2}{\theta_\Gamma^2}u_\Omega^2 & 2\frac{\theta_\Omega}{\theta_\Gamma}u_\Omega & 0 \\ -\frac{\phi_\Gamma}{\phi_\Omega}\frac{\theta_\Omega^2}{\theta_\Gamma^2}u_\Omega v_\Omega & \frac{\theta_\Omega}{\theta_\Gamma}v_\Omega & \frac{\theta_\Omega}{\theta_\Gamma}u_\Omega \end{bmatrix} \tag{53a}$$

The eigenvalue $\frac{\theta_\Omega}{\theta_\Gamma}u_\Omega$ stems directly from the third column of the matrix. The remaining two are those of the 2×2 matrix

$$\mathbf{B}_x = \begin{bmatrix} 0 & 1 \\ \frac{\theta_\Gamma}{\theta_\Omega}c_\Omega^2 - \frac{\phi_\Gamma}{\phi_\Omega}\frac{\theta_\Omega^2}{\theta_\Gamma^2}u_\Omega^2 & 2\frac{\theta_\Omega}{\theta_\Gamma}u_\Omega \end{bmatrix} \tag{54}$$

with determinant

$$\det \mathbf{B}_x = \frac{\phi_\Gamma}{\phi_\Omega}\frac{\theta_\Omega^2}{\theta_\Gamma^2}u_\Omega^2 - \frac{\theta_\Gamma}{\theta_\Omega}c_\Omega^2 \tag{55}$$

and eigenvalues

$$\lambda = \frac{\theta_\Omega}{\theta_\Gamma}u_\Omega \pm \left(\left(\frac{\theta_\Omega}{\theta_\Gamma} \right)^2 \left(1 - \frac{\phi_\Gamma}{\phi_\Omega} \right) u_\Omega^2 + \frac{\theta_\Gamma}{\theta_\Omega}c_\Omega^2 \right)^{1/2} \tag{56}$$

hence the eigenvalues given in Equation (28c). Hyperbolicity is guaranteed provided that $\phi_\Gamma \leq \phi_\Omega$. If the porosity is depth-independent, the above expression simplifies to:

$$\lambda = \frac{\phi_\Omega}{\phi_\Gamma}u_\Omega \pm \left(\left(\frac{\phi_\Omega}{\phi_\Gamma} \right) \left(\frac{\phi_\Omega}{\phi_\Gamma} - 1 \right) u_\Omega^2 + \frac{\phi_\Gamma}{\phi_\Omega}c_\Omega^2 \right)^{1/2} \tag{57}$$

Appendix B. Approximate Riemann solver

The purpose of this Appendix is to present a justification for the mass flux formula (33a) in the modified HLLC [46] Riemann solver. The principles of the Riemann solver can be found elsewhere [45] and will not be recalled here. This formula is developed bearing two objectives in mind. Firstly, the C-property [3]

$$\left.\begin{array}{c} z_{s,\Gamma,L} = z_{s,\Gamma,R} \\ q_L = q_R = 0 \end{array}\right\} \Rightarrow q_{ij} = 0 \tag{58}$$

must be verified. Secondly, the particular situations where one of the domain porosities $\phi_{\Gamma,L}$, $\phi_{\Gamma,R}$ is zero must yield a zero discharge. From a physical point of view, a zero porosity is the sign that no additional mass can be stored within the domain under a unit rise in the water level. This is the case when the water level is below the bed level in free surface flow, or above the lid of a conduit for pipe flow. Applying the HLL [26] approach to the continuity equation gives the following two conditions

$$q_L - q_{ij} = (\theta_{\Gamma,L} - \theta_{ij})\,\lambda^- \tag{59a}$$

$$q_{ij} - q_R = (\theta_{ij} - \theta_{\Gamma,R})\,\lambda^+ \tag{59b}$$

$$\theta_{\Gamma,S} = \theta_\Gamma\left(z_{s,\Gamma,S}\right), \quad S = L, R \tag{59c}$$

where $\lambda^\pm$ are the (a priori estimated) speeds of the discontinuities that separate the intermediate region of constant state from the left and right states of the Riemann problem. Solving the above equations for q_{ij} yields

$$q_{ij} = \frac{\lambda^+ q_L - \lambda^- q_R}{\lambda^+ - \lambda^-} - \frac{\lambda^+\lambda^-}{\lambda^+ - \lambda^-}\left(\theta_{\Gamma,L} - \theta_{\Gamma,R}\right) \tag{60}$$

Equation (60) satisfies the C-property because the condition $(z_{s,\Gamma,L} = z_{s,\Gamma,R})$ automatically yields $\theta_{\Gamma,L} = \theta_{\Gamma,R}$.

However, this equation is not entirely satisfactory in that it does not allow the following particular case to be accounted for. Assume the following situation

$$z_{b,\Gamma,L} < z_{s,\Gamma,L} < z_{s,\Gamma,R} \tag{61a}$$

$$z_{s,\Gamma,R} = z_{b,\Gamma,R} \tag{61b}$$

$$q_L \neq 0, \quad q_R = 0 \tag{61c}$$

In this situation the left-hand side of the interface is immersed, while the right-hand side is emerged. In such a case, a zero discharge should be obtained because the water cannot flow across the interface. However, Equation (60) allows for $q_{ij} \neq 0$ in such a case. Indeed, one has

$$\lambda^- = \lambda_1\left(q_L, z_{s,\Gamma,L}\right) < 0 \tag{62a}$$

$$\lambda^+ = \lambda_3\left(q_L, z_{s,\Gamma,L}\right) > 0 \tag{62b}$$

$$\theta_{\Gamma,L} = \theta_{\Gamma,R} = 0 \tag{62c}$$

leading to a non-zero discharge q_{ij}. Note that the third equation is obtained from the condition (2d), with $\theta_{\Omega,R} = 0$.

The solver is modified as follows. Noticing that $\mathrm{d}\theta = \phi \mathrm{d}z$ and that the laws $\phi(z)$ are discretized as piecewise constant functions (Subsection 3.2, Equations (35a, 35b)), the balance equations are replaced with the following approximate relationships

$$q_L - q_{ij} = (z_{s,\Gamma,L} - z_{s,ij})\,\phi_{\Gamma,L}\lambda^- \tag{63a}$$

$$q_{ij} - q_R = (z_{s,ij} - z_{s,\Gamma,R})\,\phi_{\Gamma,R}\lambda^+ \tag{63b}$$

Solving this system for q_{ij} leads to Equation (33a). With this formula, the configuration (61a-61c) leads to $\phi_{\Gamma,R} = 0$, thus yielding $q_{ij} = 0$. The C-property (58) is also verified.

References

[1] Bates, P.D. 2000. Development and testing of a subgrid-scale model for moving-boundary hydrodynamic problems in shallow water. Hydrological Processes 14, 2073-2098.

[2] Benkhaldoun, F., Elmahi, I., Moumna, A., Seaid, M. 2016. A non-homogeneous Riemann solver for shallow water equations in porous media. Applicable Analysis 95, 2181-2202. doi: 10.1080/00036811.2015.1067304.

[3] Bermudez, A., Vazquez, M.E. 1994. Upwind methods for hyperbolic conservation laws with source terms. Computers & Fluids 8, 1049-1071.

[4] Bernardini, G., Postacchini, M., Quagliarini, E., Brocchini, M., Cianca, C., D'Orazio, M., 2017. A preliminary combined simulation tool for the risk assessment of pedestrians' flood-induced evacuation. Environmental Modelling & Software 96, 14-29, 2017.

[5] Boutron, O., Bertrand, O., Fiandrino, A., Höhener, P., Sandoz, A., Chérain, Y., Coulet, E., Chauvelon, P. 2015. An unstructured numerical model to study wind-driven circulation patterns in a managed coastal mediterranean wetland: the Vaccarès lagoon system. Water 7, 5986-6016.

[6] Bruwier, M. Archambeau, P. Erpicum, S. Pirotton, M. Dewals, B. 2017. Shallow-water models with anisotropic porosity and merging for flood modelling on Cartesian grids. Journal of Hydrology 554, 693-709.

[7] Candela, A., Noto, L.V., Aronica, G. 2005. Influence of surface roughness in hydrological response of semiarid catchments. Journal of Hydrology 313, 119-131.

[8] Cea, L., Vazquez-Cendon, M.E. 2010. Unstructured finite volume discretization of two-dimensional depth-averaged shallow water equations with porosity. Int J Numer Methods Fluids 63, 903–30.

[9] Chapman, J.A, Wilson, B.N., Gulliver, J.S. 2015. Drag force parameters of rigid and flexible vegetal elements. Water Resources Research, 51, 3292-3302.

[10] Chen, A.S., Evans, B., Djordjevic, S., Savic, D., 2012a. A coarse-grid approach to representing building blockage effects in 2D urban flood modelling. Journal of Hydrology 426, 1-16.

[11] Chen A., Evans B., Djordjevic S., Savic D.A., 2012b. Multi- layer coarse- grid modelling in 2D urban flood simulations, J . Hydrol. 470, 1–11.

[12] Davis, S.F. 1988. Simplified Second-order Godunov-type methods. SIAM Journal of Scientific and Statistical Computing 9, 445-473.

[13] Defina, A. 2000. Two-dimensional shallow flow equations for partially dry areas. Water Resour Res 2000; 36: 3251–64.

[14] Defina, A., Bixio, A.C. 2005. Mean flow and turbulence in vegetated open channel flow. Water Resources Research, 41, W07006.

[15] Ferrari, A., Vacondio, R., Dazzi, S., Mignosa, P., 2017. A 1D-2D shallow water equation solver for discontinuous porosity field based on a Generalized Riemann problem. Advances in Water Resources 107, 233-249.

[16] Ferrarin, C., Umgiesser, G., 2005. Hydrodynamic modeling of a coastal lagoon: the Cabras lagoon in Sardinia, Italy. Ecological Modelling 188, 340-357.

[17] Finaud-Guyot, P., Delenne, C., Lhomme, J., Guinot, V., Llovel, C. 2010. An approximate-state Riemann solver for the two-dimensional shallow water equations with porosity. International Journal for Numerical Methods in Fluids 62, 1299–1331.

[18] Fraga, I., Cea, L., Puertas, J. 2013. Experimental study of the water depth and rainfall intensity effects on the bed roughness coefficient used in distributed urban drainage models. Journal of Hydrology 505, 266-275.

[19] Godunov, S.K. 1959. A difference method for numerical calculation of discontinuous equations of hydrodynamics. Matematicheski Sbornik 47:271{300 (in Russian).

[20] Guinot, V. 2010. Wave propagation in fluids. Models and numerical techniques. 2nd edition. Wiley-ISTE.

[21] Guinot, V. 2012. Multiple porosity shallow water models for macroscopic modelling of urban floods. Advances in Water Resources 37, 40-72.

[22] Guinot, V. 2017a. Consistency and bicharacteristic analysis of integral shallow water models with porosity. Explaining model oversensitivity to mesh design. Advances in Water Resources 107, 34-55.

[23] Guinot, V. 2017b. A critical assessment of flux and source term closures in shallow water models with porosity for urban flood simulations. Advances in Water Resources, 109,133-157.

[24] Guinot, V., Sanders, B.F., Schubert, J. 2017. Dual integral porosity shallow water model for urban flood modelling. Advances in Water Resources 103, 31-54. DOI: 10.1016/j.advwatres.2017.06.008.

[25] Guinot, V., Soares-Frazão, S. 2006. Flux and source term discretization in shallow water models with porosity on unstructured grids. Int J Numer Methods Fluids 50, 309–45.

[26] Harten, A., Lax, P.D., Van Leer, B. 1983. On upstream differencing and Godunov type methods for hyperbolic conservation laws. SIAM review . 25(1): 35 - 61.

[27] Katz D.M., Watts F.J., Burroughs E.R. 1995. Effect of surface roughness and rainfall impact on overland flow. Journal of Hydraulic Engineering 121, 546-553.

[28] Kim, D.H., Lynett, P.J., Socolofsky, S.A. 2009. A depth-integrated model for weakly dispersive, turbulent, and rotational fluid flows. Ocean Modelling, 27, 198-214.

[29] Kim, B., Sanders, B.F., Famiglietti, J.S., Guinot, V. 2015. Urban flood modeling with porous shallow-water equations: A case study of model errors in the presence of anisotropic porosity. Journal of Hydrology 523, 680-692.

[30] Kouwen, N., Unny, T.E., Hill, H.M. 1969. Flow retardance in vegetated channels. Journal of the Irrigation and Drainage Division 95, 329-342.

[31] Lawrence, D.S.L. 1997. Macroscale surface roughness and frictional resistance in overland flow. Earth Surface Processes and Landforms 22, 365-382.

[32] Liang D, Falconer RA, Lin B. 2007. Coupling surface and subsurface flows in a depth averaged flood wave model. J Hydrol 337, 147–58.

[33] Nepf, H.M. 1999. Drag, turbulence, and diffusion in flow through emergent vegetation. Water Resources Research, 35, 479-489.

[34] Özgen, I., Liang, D., Hinkelmann, R. 2016. Shallow water equations with depth-dependent anisotropic porosity for subgrid-scale topography. Applied Mathematical Modelling 40, 7447- 7473.

[35] Özgen, I., Liang, D., Hinkelmann, R. 2016. Urban flood modeling using shallow water equations with depth-dependent anisotropic porosity. J. Hydrol. 541, 1165–1184 .

[36] Özgen, I. Teuber, K., Simons, F., Liang, D., Hinkelmann, R. 2015. Upscaling the shallow water model with a novel roughness formulation. Environmental Earth Sciences, 74, 7371-7386.

[37] Park, H., Cox, D.T., Lynett, P.J., Wiebe D.M., Shin, S. 2013. Tsunami inundation modeling in constructed environments: A physical and numerical comparison of free-surface elevation, velocity, and momentum flux. Coastal Engineering, 79, 9-21.

[38] Sanders, B.F., Schubert, J.E., Gallegos, H.A. 2008. Integral formulation of shallow water equations with anisotropic porosity for urban flood modelling. J Hydrol 362, 19–38.

[39] Schubert, J.E. , Sanders, B.F. 2012. Building treatments for urban flood inundation models and implications for predictive skill and modeling efficiency. Adv. Water Resour. 41, 49–64 .

[40] Siniscalchi, F., Nikora, V.I., Aberle, J. 2012. Plant patch hydrodynamics in streams: mean flow, turbulence, and drag forces. Water Resources Research, 48, W01513.

[41] Soares-Frazão, S., Guinot, V. 2007. An eigenvector-based linear reconstruction scheme for the shallow water equations on two-dimensional unstructured meshes. International Journal for Numerical Methods in Fluids 53, 23–55.

[42] Soares-Frazão, S., Lhomme, J., Guinot, V., Zech, Y. 2008. Two–dimensional shallow water models with porosity for urban flood modelling. Journal of Hydraulic Research 46(1), 45-64.

[43] Strang, G. 1968. On the construction and comparison of difference schemes. SIAM Journal of Numerical Analysis 5, 506-517.

[44] Tayfur, G., Kawas, M.L., Govindaraju, R.S., Storm, D.E. 1993. Applicability of St. Venant equations for two-dimensional overland flow over rough infiltrating surfaces. Journal of Hydraulic Engineering 119, 51-63.

[45] Toro, E.F.. 1997. Riemann solvers and numerical methods for fluid dynamics. Springer.

[46] Toro, E.F., Spruce, M., Speares, W. 1994. Restoration of the contact surface in the HLL-Riemann solver. Shock Waves 4, 25-34.

[47] Velickovic, M., Zech, Y., Soares-Frazão, S. 2017. Steady-flow experiments in urban areas and anisotropic porosity model. Journal of Hydraulic Research 55, 85-100.

[48] Viero, D.P., Valipour, M. 2017. Modeling anisotropy in free-surface overland and shallow inundation flows. Advances in Water Resources 104, 1-14.

[49] Volp, N.D., van Prooijen, B.C., Stelling, G.S., 2013. A finite volume approach for shallow water flow accounting for high-resolution bathymetry and roughness data. Water Resources Research 49, 4126-4135.

[50] Wilson C.A.M.E., Horritt M.S. 2002. Measuring the flow resistance of submerged grass. Hydrological Processes 16, 2589-2598.